nature portfolio

https://doi.org/10.1038/s41586-025-10062-6

Supplementary information

Cavity-altered superconductivity

In the format provided by the authors and unedited

Cavity-altered superconductivity: Supplementary Information

Itai Keren[*1,¶], Tatiana A. Webb[†1,¶], Shuai Zhang[‡1,¶], Jikai Xu[1], Dihao Sun[1], Brian S. Y. Kim[1], Dongbin Shin[2,3], Songtian S. Zhang[1], Junhe Zhang[1], Giancarlo Pereira[1], Juntao Yao[4,5], Takuya Okugawa[1,2], Marios H. Michael[2], Emil Viñas Boström[2], James H. Edgar[6], Stuart Wolf[7], Matthew Julian[7], Rohit P. Prasankumar[7], Kazuya Miyagawa[8], Kazushi Kanoda[9,10,8], Genda Gu[4], Matthew Cothrine[11], David Mandrus[11], Michele Buzzi[2], Andrea Cavalleri[2,12], Cory R. Dean[1], Dante M. Kennes[2,13], Andrew J. Millis[1,14], Qiang Li[4,15], Michael A. Sentef[16,2], Angel Rubio[2,17], Abhay N. Pasupathy[1,4], and D. N. Basov [§1]

[1]Department of Physics, Columbia University, New York, NY 10027, USA
[2]Max Planck Institute for the Structure and Dynamics of Matter, Luruper Chaussee 149, 22761 Hamburg, Germany
[3]Department of Physics and Photon Science, Gwangju Institute of Science and Technology (GIST), Gwangju 61005, Republic of Korea
[4]Condensed Matter Physics and Materials Science Division, Brookhaven National Laboratory, Upton, NY 11973, USA
[5]Department of Materials Science and Chemical Engineering, Stony Brook University, Stony Brook, NY 11794-3800, USA
[6]Tim Taylor Department of Chemical Engineering, Kansas State University, Manhattan, KS 66506, USA
[7]Deep Science Fund, Intellectual Ventures, Bellevue, WA 98007, USA
[8]Department of Applied Physics, The University of Tokyo, Bunkyo, Tokyo 113-8656, Japan
[9]Max Planck Institute for Solid State Research, Heisenbergstrasse 1, 70569 Stuttgart, Germany
[10]Physics Institute, University of Stuttgart, Pfaffenwaldring 57, 70569 Stuttgart, Germany
[11]Department of Materials Science and Engineering, University of Tennessee, Knoxville, TN 37996, USA
[12]Department of Physics, Clarendon Laboratory, University of Oxford, Oxford OX1 3PU, United Kingdom
[13]Institut für Theorie der Statistischen Physik, RWTH Aachen, 52056 Aachen, Germany and JARA - Fundamentals of Future Information Technology
[14]Center for Computational Quantum Physics, The Flatiron Institute, New York, NY, USA
[15]Department of Physics and Astronomy, Stony Brook University, Stony Brook, NY 11794-3800, USA
[16]Institute for Theoretical Physics and Bremen Center for Computational Materials Science, University of Bremen, 28359 Bremen, Germany
[17]Initiative for Computational Catalysts, The Flatiron Institute, New York, NY 10010, USA
[¶]These authors contributed equally

[*]ik2561@columbia.edu
[†]tw2864@columbia.edu
[‡]szhangphysics@gmail.com
[§]db3056@columbia.edu

1 Magnetic susceptibility of bulk κ-ET crystals

Magnetic susceptibility measurements were performed using a Quantum Design Magnetic Property Measurement System (MPMS) equipped with a superconducting quantum interference device (SQUID) magnetometer (Fig. S1). To investigate the superconducting transition, the applied magnetic field was set to 2 Oe and perpendicular to the ac plane (see crystal structure in Fig. S2).

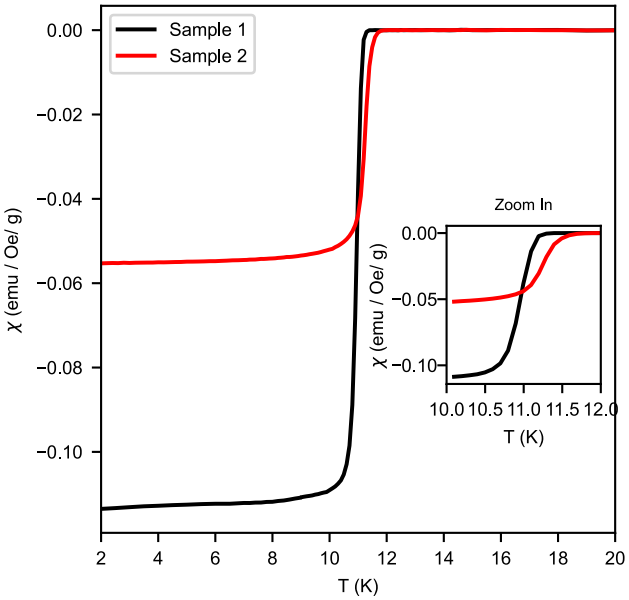

Figure S1: **T_c measured by SQUID magnetometry**. Temperature-dependent zero-field-cooled (ZFC) magnetic susceptibility for two samples measured in a 2-Oe field applied perpendicular to the ac plane. Both samples exhibit a sharp superconducting transition at approximately 11.5 K. The inset provides a magnified view of the transition region.

2 κ-ET crystal structure

The crystal structure of κ-ET is presented in Fig. S2. Dimers of BEDT-TTF molecules arranged in a triangular lattice constitute two-dimensional conducting layers. Each dimer donates an electron to the Br anions, resulting in half-filled conduction bands [Kanoda, Physica C 282, 299–302 (1997)]. This structure, characterized by metallic behavior within each layer and insulating behavior across layers [Buzzi et al., Phys. Rev. Lett. 127, 197002 (2021)], is expected to allow out-of-plane electric fields to penetrate into the κ-ET crystal.

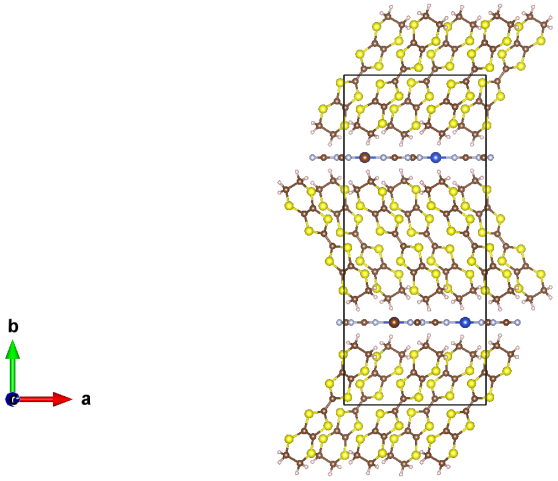

Figure S2: **κ-ET crystal structure**. A quasi-two-dimensional structure of conducting BEDT-TTF layers separated by insulating anion layers.

3 hBN slab as a cavity

In this section, we present two sets of calculations to illustrate hBN's role as a cavity. In Section 3.1, we demonstrate the frequency-selective enhancement of the photonic density of states and electric field fluctuations. In Section 3.2, we illustrate the confined modes governing hBN's response to oscillating dipolar fields within the frequency range of hyperbolicity.

3.1 Cavity electrodynamics and photonic density of states

While hyperbolic modes (HMs) in hBN are suspected to be dominated by longitudinal modes which are described by the Coulomb force [Andolina et al., Phys. Rev. B 109, 104513 (2024)], it is convenient to use the Weyl gauge in order to quantize them in a thin slab. Within the Weyl gauge, both transverse and longitudinal modes are captured through a vector potential, and the electric field is given by: $E = -\partial_t A$, with A being the vector potential. Following the method used in [Eckhardt et al., Nat. Commun. 15, 2300 (2024); Gubbin et al., Phys. Rev. B 94, 205301 (2016); Eckhardt et al., arXiv:2409.10615 (2024); Viñas Boström et al., Phys. Rev. Res. 7, 033163 (2025)], we can derive the electric field quantum fluctuations in vacuum as a consequence of linearly coupled infrared active matter degrees of freedom, such as phonons and plasmons. We generalize the previous results to the case of a hyperbolic system by using the Hamiltonian:

$$\begin{aligned} H = &\int d^3x \left(\frac{\left(\vec{E}\right) \cdot \underline{\underline{\epsilon}}_{\infty}^{-1}(x) \cdot \left(\vec{E}\right)}{2\epsilon_0} + \frac{(\nabla \times A)^2}{2\mu_0} \right) + \\ &\int d^3x g(x) \left(\frac{\rho}{2} \vec{X} \cdot \underline{\underline{\omega_{ph}^2}} \cdot \vec{X} + \frac{1}{2\rho} \vec{\Pi}^2 \right) \end{aligned} \tag{1}$$

The first term corresponds to the energies of the electric and magnetic fields, where the electric field $\vec{E} = \vec{D} - \underline{\underline{\kappa}}(x) \cdot \vec{X}$ is given in terms of the dielectric field $\vec{D}$, the phonon coordinate $\vec{X}$, and $\underline{\underline{\kappa}}(x)$, the coupling between phonon mode and light, which will be expressed below in terms of the frequency permittivity matrix. The second term corresponds to the Hamiltonian of a hyperbolic phonon where the phonon frequency becomes a matrix, $\omega_{ph}^2 = \begin{pmatrix} \omega_{\parallel}^2 & 0 & 0 \\ 0 & \omega_{\parallel}^2 & 0 \\ 0 & 0 & \omega_{\perp}^2 \end{pmatrix}$, $\vec{X}$ and $\vec{\Pi}$ are the coordinate and momentum of the phonon, and ρ is the ion density contributing to the phonon. $\underline{\underline{\epsilon}}_{\infty}^{-1} = \begin{pmatrix} 1/\epsilon_{\infty,\parallel} & 0 & 0 \\ 0 & 1/\epsilon_{\infty,\parallel} & 0 \\ 0 & 0 & 1/\epsilon_{\infty,\perp} \end{pmatrix}$. The spatial dependence of $\underline{\underline{\epsilon}}^{-1}(x)$ and $g(x)$ define the region of the hBN thin slab: $g(x) = 1$ inside the crystal and $g(x) = 0$ outside, while $\epsilon = 1$ outside the slab for a slab in air. Finally, the quantum fluctuations are given through the commutation relations of the quantum operators:

$$\left[\vec{D}_i(x), \vec{A}_j(x')\right] = i\delta_{i,j}\delta^3(x - x'), \qquad \left[\vec{X}_i(x), \vec{\Pi}_j(x')\right] = i\delta_{i,j}\delta^3(x - x') \tag{2}$$

The equations of motion of the phonon in response to light are given by:

$$\partial_t \vec{X} = \frac{\vec{\Pi}}{\rho} \tag{3}$$

$$\left(\partial_t^2 + \underline{\underline{\omega_{ph}^2}}\right) \cdot \vec{X} = \frac{1}{\rho} \underline{\underline{\kappa}} \cdot \vec{E} \tag{4}$$

The equations of motion of light in the presence of the phonon coordinate come from the Maxwell equations:

$$\partial_t \vec{A} = -\vec{E} \tag{5}$$

$$\partial_t \vec{D} = \nabla \times \nabla \times \vec{A} \tag{6}$$

Solving this set of equations allows us to derive the eigenmodes:

$$\vec{A}(x,t) = \sum_i \left(\vec{f}_i(x) e^{-i\omega_i t} \hat{a}_i + \vec{f}_i^*(x) e^{i\omega_i t} \hat{a}_i^\dagger \right) \tag{7}$$

The electric field fluctuations can be computed through $E = -\partial_t A$:

$$\vec{E}(x,t) = \sum_i \left(i\omega_i \vec{f}_i(x) e^{-i\omega_i t} \hat{a}_i - i\omega_i \vec{f}_i^*(x) e^{i\omega_i t} \hat{a}_i^\dagger \right) \tag{8}$$

The equations of motion specify the eigenvectors $\vec{f}_i(x)$ up to an overall normalization factor. The eigenvector used in this calculation follows the eigenvectors in [Ashida et al., Phys. Rev. Lett. 130, 216901 (2023)]. The normalization factor can be derived by requiring that the creation and annihilation operators have standard bosonic commutation relations:

$$\left[a_i, a_j^\dagger\right] = \delta_{i,j} \tag{9}$$

This leads to the following normalization condition [Eckhardt et al., Nat. Commun. 15, 2300 (2024); Eckhardt et al., arXiv:2409.10615 (2024); Gubbin et al., Phys. Rev. B 94, 205301 (2016)]:

$$\epsilon_0 \omega_i \int d^3x \left(\vec{f}_i \cdot \underline{\underline{v(\omega,x)\epsilon(\omega,x)}} \cdot \vec{f}_i \right) = 1 \tag{10}$$

In the diagonal basis $\{x, y, z\}$, the matrix is given by:

$$\underline{\underline{v(\omega,x)\epsilon(\omega,x)}}_i = v_i(\omega,x)\epsilon_i(\omega,x) \tag{11}$$

$$\text{with} \quad v_i(\omega,x) = 2 + \frac{\omega}{\epsilon_i(\omega,x)} \partial_\omega \left(\epsilon_i(\omega,x)\right) \tag{12}$$

The matrix v captures the fraction of the eigenmode that resides within the matter degrees of freedom as opposed to the light degrees of freedom. ϵ_i is the permittivity in the i-th direction (x,y,z) in the diagonal basis. The permittivity of the HMs is obtained by solving the equations of motion and is given by:

$$\epsilon_\parallel(w) = \epsilon_{\text{inf},\parallel}(1 - \omega_{pl,\parallel}^2/(\omega^2 + i\gamma_\parallel\omega - \omega_\parallel^2)) \qquad \text{and} \qquad \epsilon_\perp(\omega) = \epsilon_{\text{inf},\perp}(1 - \omega_{pl,\perp}^2/(\omega^2 + i\gamma_\perp\omega - \omega_\perp^2)) \tag{13}$$

We use the appropriate numbers for hBN described in [Nazaryan et al., arXiv:2402.15563 (2024)]: $\omega_\perp = 23.3$ THz, $\omega_\parallel = 41.1$ THz, $\omega_{pl,\perp} = (0.37 * \omega_\perp), \omega_{pl,\parallel} = (0.61 * \omega_\parallel), \epsilon_\perp = 2.95, \epsilon_\parallel = 4.87$. Within the quantum calculation, we work in the limit of $\gamma_\perp = \gamma_\parallel = 0$. Putting everything together, the electric field fluctuations for a specific cavity geometry are given by:

$$\langle E^i E^j(x,t)\rangle_0 = \sum_n \omega_n^2 f_n^i(x) f_n^j(x) \equiv \int d\omega \omega \rho_{i,j}(\omega,x) \tag{14}$$

The frequency-dependent partial local density of states (PLDOS), $\rho_{i,j}(\omega,x)$ is defined as:

$$\rho_{i,j}(\omega,x) = \sum_n \omega_n f_n^i(x) f_n^j(x) \delta(\omega - \omega_n). \tag{15}$$

The term partial local density of states refers to the photonic part of the polariton modes for specific spatial orientation at a position in space. With this, we define electric field fluctuations per unit of frequency as :

$$\langle E_i E_j\rangle(\omega,x) = \omega \rho_{i,j}(\omega,x) \tag{16}$$

Note that the ratio of the PLDOS of a photonic structure compared to that of free space, which is usually calculated for photonic systems [Glauber and Lewenstein, Phys. Rev. A 43, 467 (1991)], equals the ratio of electric field fluctuations in vacuum compared to free space:

$$\frac{\langle E_i E_j\rangle_{\text{cav}}(\omega,x)}{\langle E_i E_j\rangle_{\text{free space}}(\omega)} = \frac{\rho_{\text{cav}}(\omega,x)}{\rho_{\text{free space}}(\omega)} \tag{17}$$

Fundamentally, cavities modify the dispersion of light from free space (Fig. S3b, e, and h). The altered dispersions generate the frequency-selective enhancement of the PLDOS and field fluctuations described above. In Fig. S3, we present this behavior for both hBN and a typical Fabry-Pérot resonator. The Fabry-Pérot enhancement has a maximum of 3 for any frequency. Hyperbolic hBN, by contrast, offers orders of magnitude of enhancement, far exceeding those of Fabry-Pérot geometries at the same frequency.

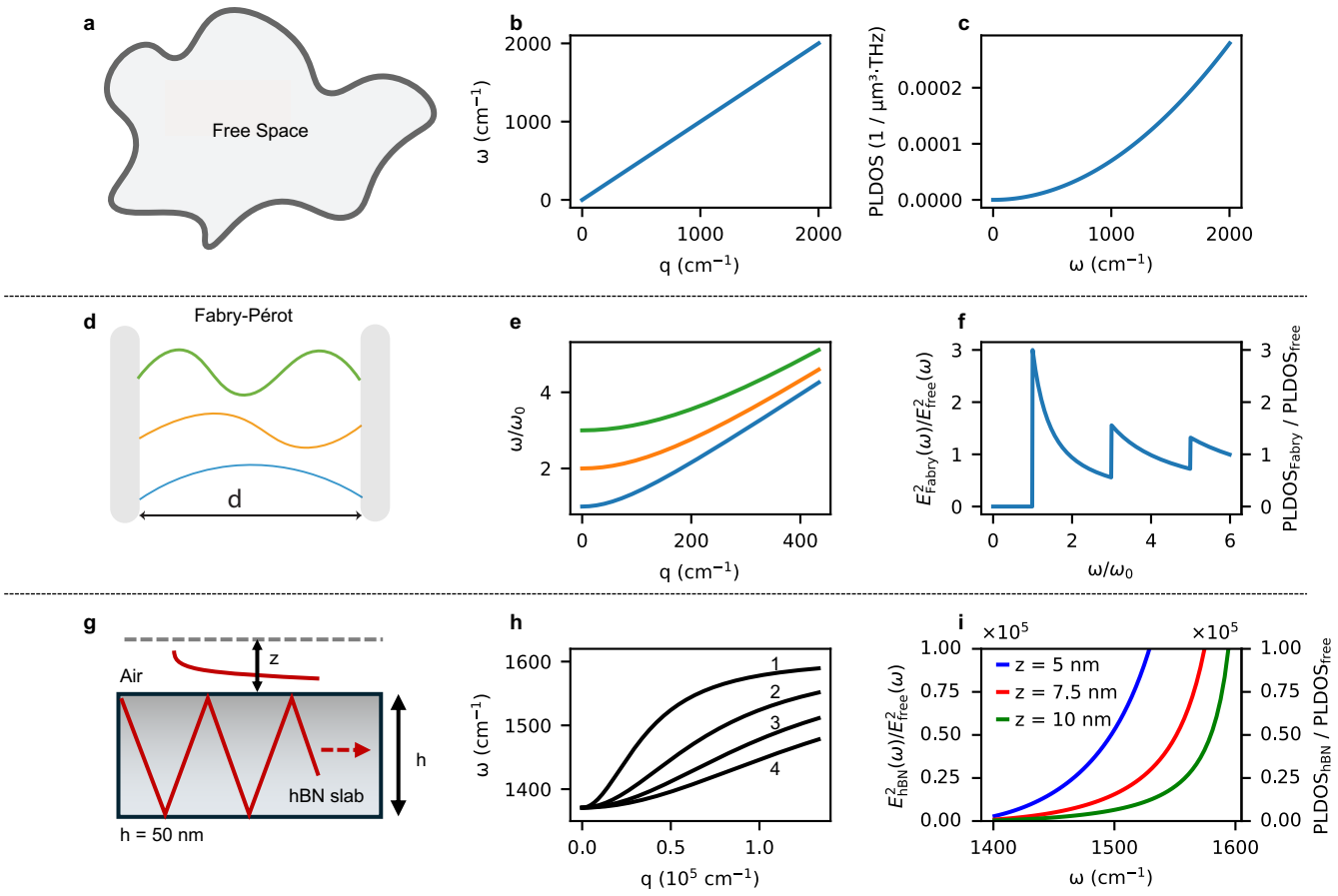

Figure S3: **Electromagnetic cavities: hBN and Fabry-Pérot resonators. a-c,** schematic (a), dispersion (b), and PLDOS (c) of free space. **d-f,** schematic (d), dispersion (e), and electric field fluctuations normalized by the free-space fluctuations (f) in a Fabry-Pérot cavity. The secondary y-axis in (f) displays the PLDOS relative to the free-space PLDOS. **g-i,** same as d-f in the setting of a 50-nm-thick hBN slab. In panel h, curves labeled 1-4 correspond to dispersion branches 1-4. The nth branch exhibits $n-1$ nodes within the hBN microcrystal. In panel (i), the electric field fluctuations are calculated for three different heights z above the hBN slab.

3.2 Electric field of an hBN slab near an oscillating dipole

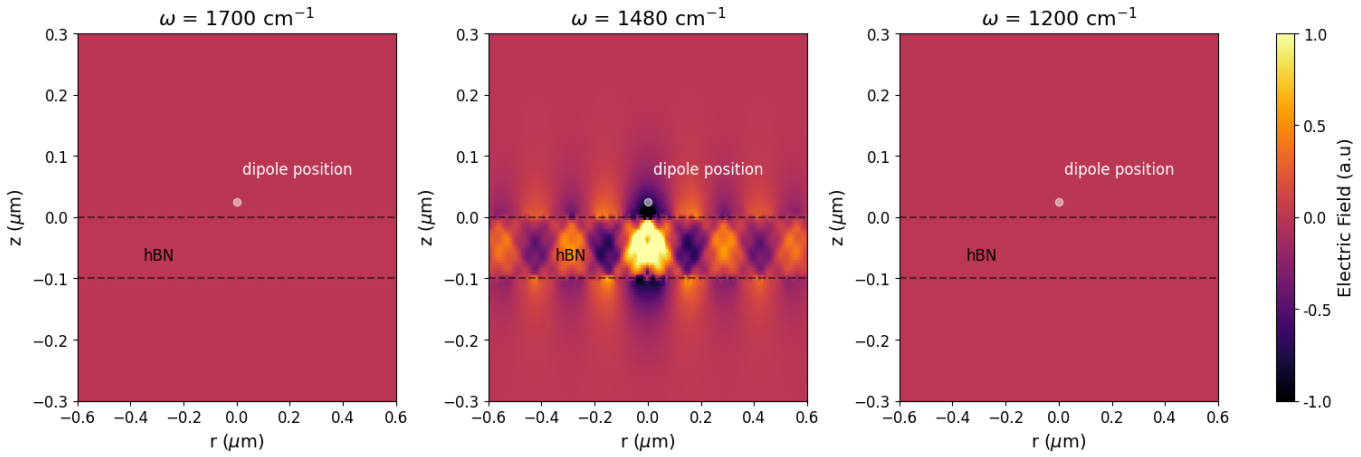

Figure S4: **hBN slab in the proximity of an oscillating electric point dipole**. Two-dimensional false-color plot of Re $\left[\tilde{E}_{\mathrm{hBN},z}(r,z)\right]$ as a function of r and z for three different frequencies ω. $\omega = 1480$ cm^{-1} lies within the hyperbolic regime of hBN, whereas $\omega = 1700, 1200$ cm^{-1} do not. The corresponding dielectric constants are listed in Table 1.

Table 1: **hBN dielectric constants for different frequencies.** Values of the dielectric constants were estimated from [Giles et al., Nat. Mater. 17, 134 (2018)].

frequency [cm^{-1}]	ϵ_r	ϵ_z
1480	−10	5
1700	1	5
1200	10	5

We now present an explicit example of an hBN slab acting as an electromagnetic cavity. To this end, we compute the time-harmonic electromagnetic field distributions using the Electromagnetic Waves, Frequency Domain interface of the Wave Optics Module in COMSOL Multiphysics. We consider a system where an hBN slab is placed in a vacuum and an oscillating electric point dipole is located 25 nm above the hBN surface, oriented along the z-direction [Guo et al., J. Appl. Phys. 127, 071101 (2020)]. The thickness of the hBN slab is 100 nm. Since the system has rotational symmetry about the point dipole, we use cylindrical coordinates and apply circular symmetry for numerical computation. The central surface of the hBN is set at the origin, and the hBN radius is 0.6 μm. A vacuum domain is created beneath the hBN extending 1 μm from the hBN surface. In addition, a hemispherical vacuum domain of radius 1 μm is included above the slab. To suppress spurious electromagnetic reflection from the computational boundary, we implement a perfectly matched, 250-nm-thick layer at each boundary of the geometry. The electric dipole moment is pointed along the $z-$direction and is set to 1 A·m.

We compute the electric field in both the presence and the absence of hBN (denoted $\boldsymbol{E}_{\mathrm{hBN+dip}}$ and $\boldsymbol{E}_{\mathrm{dip}}$, respectively). In the latter case, the hBN domain is replaced by vacuum. The electric field induced purely by hBN is obtained using the relationship $\boldsymbol{E}_{\mathrm{hBN}} = \boldsymbol{E}_{\mathrm{hBN+dip}} - \boldsymbol{E}_{\mathrm{dip}}$. We compute the spatial profile of the electric field for three dipole frequencies: 1700 cm^{-1}, 1480 cm^{-1}, and 1200 cm^{-1}. The corresponding dielectric functions are taken from experimental measurements, as summarized in Table 1. The resulting map of Re $\left[\tilde{E}_{\mathrm{hBN},z}(r,z)\, e^{i\omega t}\right]$ at $t = 0$ are shown in Fig. S4. Note that $\tilde{E}_{\mathrm{hBN},z}(r,z)$ is a complex-valued function. Within the hyperbolic frequency range of hBN, confined hyperbolic phonon-polariton (HPhP) modes appear within the hBN volume and their associated electric field extends well beyond the hBN surface.

4 hBN/κ-ET heterostructures

The device geometries for the six κ-ET-based devices studied in this work are shown in Fig. S5.

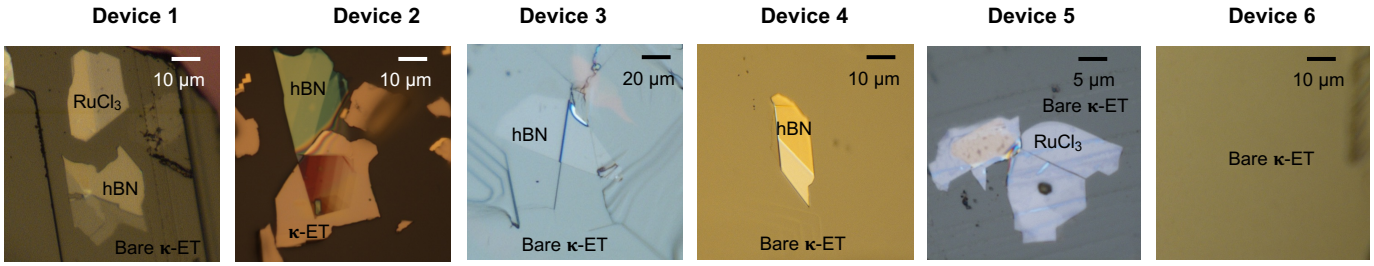

Figure S5: **κ-ET devices**. Optical images of the κ-ET devices, as described in the Methods section, based on as-grown κ-ET single-crystal surfaces (Devices 1, 4, and 5), an exfoliated κ-ET microcrystal (Device 2), and cleaved κ-ET single-crystal surfaces (Devices 3 and 6). The optical contrast shows steps in the κ-ET crystal surfaces and variations in the 2D materials' layer thicknesses.

5 Quantitative determination of the superfluid density from MFM

Fitting the force gradient $\partial_z F_z(z)$ experienced by the tip at different locations on bare κ-ET across multiple devices to a London-theory model gives a penetration depth for in-plane screening currents of $\lambda_{\text{in}}(2\text{K}) = 660 \pm 110$ nm, within the range of previous measurements obtaiend using muon spin relaxation [Le et al., Phys. Rev. Lett. 68, 1923 (1992); Carrington et al., Phys. Rev. Lett. 83, 4172 (1999)] and microwave surface impedance [Milbradt et al., Phys. Rev. B 88, 064501 (2013)]. In this work, we assume the superfluid density $\rho \propto \lambda_{\text{in}}^{-2}$.

In this section, we describe the London-theory model of $\partial_z F_z$ and how it was applied to extract λ_{in} (or, equivalently, the superfluid density) from $\partial_z F_z(z)$ curves and $\partial_z F_z(x, y)$ MFM images.

5.1 London-theory model of $\partial_z F_z$

To solve for $\partial_z F_z$, we use the Green's function method and consider a magnetic dipole above a bulk superconductor with uniform λ_{in}. We apply London's equations for the superconducting half-infinite space at $z < 0$ and Maxwell's equations outside the superconductor [Xu et al., Phys. Rev. B 51, 424 (1995)]:

$$\nabla^2 \mathbf{A} = \begin{cases} \mathbf{A}/\lambda_{\text{in}}^2 & z < 0 \\ \mu_0 m \hat{\boldsymbol{z}} \times \nabla \delta^3 \left(\boldsymbol{r} - \boldsymbol{r}_{\text{dip}} \right) & z > 0 \end{cases} \tag{18}$$

where $\mathbf{A}$ is the vector potential and $\boldsymbol{r}_{\text{dip}} = (\rho = 0, \theta = 0, z = a)$ is the location (in cylindrical coordinates) of a magnetic dipole above the superconductor; this gives us the preliminary model of our tip.

To distinguish the dipole field from the induced field, we separate the total vector potential into $\boldsymbol{A}_{\text{dip}}$ and $\boldsymbol{A}_{\text{ind}}$ outside the superconductor:

$$\boldsymbol{A} = \begin{cases} \boldsymbol{A}_{\text{sc}} & z < 0 \\ \boldsymbol{A}_{\text{dip}} + \boldsymbol{A}_{\text{ind}} & z > 0 \end{cases} \tag{19}$$

where the dipole field satisfies $\nabla^2 \boldsymbol{A}_{\text{dip}} = \mu_0 m \hat{\boldsymbol{z}} \times \nabla \delta^3 (\boldsymbol{r} - \boldsymbol{r}_{\text{dip}})$ and the induced field $\boldsymbol{A}_{\text{ind}}$ is the corresponding homogeneous solution to $\nabla^2 \boldsymbol{A}_{\text{ind}} = 0$. The dipole vector potential has the well-known form

$$\boldsymbol{A}_{\text{dip}} = \frac{\mu_0 m}{4\pi} \frac{\rho}{\left(\rho^2 + (z - a)^2 \right)^{3/2}} \tag{20}$$

We apply the inverse Laplace transform from the $|z - a|$ domain to the k domain and use separation of variables to solve

Eq. 18:

$$\boldsymbol{A}_{\mathrm{dip}} = \hat{\boldsymbol{\theta}} \int_0^\infty k J_1(k\rho) e^{-k|z-a|}\, \mathrm{d}k \tag{21}$$

$$\boldsymbol{A}_{\mathrm{ind}} = \hat{\boldsymbol{\theta}} \int_0^\infty C_{\mathrm{ind}}(k) J_1(k\rho) e^{-kz}\, \mathrm{d}k \tag{22}$$

$$\boldsymbol{A}_{\mathrm{sc}} = \hat{\boldsymbol{\theta}} \int_0^\infty C_{\mathrm{sc}}(k) J_1(k\rho) e^{\sqrt{k^2+\lambda_{\mathrm{in}}^{-2}}z}\, \mathrm{d}k \tag{23}$$

where $\hat{\boldsymbol{\theta}}$ is the azimuthal unit vector conventionally defined in cylindrical coordinates and $J_n(x)$ is the nth-order Bessel function of the first kind.

By matching the boundary conditions at $z = 0$

$$\nabla \times \boldsymbol{A}\left(\rho, \theta, z = 0^+\right) = \nabla \times \boldsymbol{A}\left(\rho, \theta, z = 0^-\right) \tag{24}$$

we solve for the coefficient $C_{\mathrm{ind}}(k)$ and find the induced vector potential to be

$$\boldsymbol{A}_{\mathrm{ind}} = \hat{\boldsymbol{\theta}} \int_0^\infty k \frac{k\lambda_{\mathrm{in}} - \sqrt{k^2\lambda_{\mathrm{in}}^2 + 1}}{k\lambda_{\mathrm{in}} + \sqrt{k^2\lambda_{\mathrm{in}}^2 + 1}} J_1(k\rho) e^{-k(z+a)}\, \mathrm{d}k \tag{25}$$

the vertical force from the induced repulsive field on the magnetic dipole to be

$$F_z = -\frac{\partial}{\partial z}\left(-m\hat{\boldsymbol{z}} \cdot \boldsymbol{B}\right) = m\frac{\partial}{\partial z} B_z \tag{26}$$

and the z-component of the force gradient to be

$$\frac{\partial F_z}{\partial z} = \frac{\mu_0 m^2}{4\pi} \int_0^\infty \frac{k\lambda_{\mathrm{in}} - \sqrt{k^2\lambda_{\mathrm{in}}^2 + 1}}{k\lambda_{\mathrm{in}} + \sqrt{k^2\lambda_{\mathrm{in}}^2 + 1}} k^4 e^{-k(z+a)} J_0(k\rho)\, \mathrm{d}k \tag{27}$$

The tip is modeled as a single magnetic domain with a uniform magnetic moment density on the surface of the tip. Therefore, to obtain the total $\partial_z F_z$ using the principle of superposition, we integrate with respect to z and with respect to a (the dipole height above the superconductor surface) successively over the volume of the magnetic coating. Note that the magnetic dipoles act both as a perturbation inducing a magnetic response in the superconductor and as a sensor, using the resulting magnetic force.

We consider two different geometries for the tip, as shown in Fig. S6b (inset). The cone model is described by the half-apex angle α, and the cone+cylinder model (a truncated cone with a cylinder at the apex) is described by the truncation length Δh_1, the cylinder length Δh_2, and the half-apex angle α. Based on scanning electron microscope (SEM) images of four different MFM tips, we determined a single representative model (a single set of parameters) for each tip geometry. We found tip-to-tip variation to be less significant than the overall accuracy of the approximate model geometry, justifying the use of these two models for all tips. For the cone model, we used $\alpha = 0.39$ rad. For the cone+cylinder model, we used $\Delta h_1 = 195.9$ nm, $\Delta h_2 = 307.8$ nm, and $\alpha = 0.388$ rad.

Integrating the solution Eq. (4) over the volume of the magnetic coating, we obtain the total z-component of the force gradient for the entire tip:

$$\frac{\partial F_z}{\partial z} = D \int_0^\infty k^4 \frac{k\lambda_{\mathrm{in}} - \sqrt{k^2\lambda_{\mathrm{in}}^2 + 1}}{k\lambda_{\mathrm{in}} + \sqrt{k^2\lambda_{\mathrm{in}}^2 + 1}} \left(\int_S e^{-kz'}\, \mathrm{d}\sigma\right)^2 \mathrm{d}k + \zeta z + \eta, \tag{28}$$

where we have approximated $e^{-kz} J_0(k\rho) \approx e^{-kz}$ on the surface of a cone with apex angle similar to those of the tips we use. S denotes the surface of the tip. Constant factors, including the coating thickness and the magnetic moment density, are assimilated into D, which we treat as a fitting parameter. The linear background ζ accounts for non-Meissner background forces and the constant background η accounts for the zero reference of the phase-locked loop used to measure the resonance frequency shift of the cantilever.

As the penetration depth λ_{in} increases (e.g., as $T \to T_c$), the diamagnetic repulsion becomes weaker, resulting in a flattening of the $\partial_z F_z(z)$ curve, as observed in Fig. S6a.

5.2 Extracting the superconducting penetration depth from MFM $\partial_z F_z(z)$ data

We use Eq. 28 to fit the $\partial_z F_z$ measurements with four fitting parameters: the overall factor D, the in-plane penetration depth λ_{in}, a linear background ζ to account for the non-Meissner forces, and a constant η to account for an offset in $\partial_z F_z$ associated with the zero reference of the phase-locked loop used for frequency shift measurements. While the $\partial_z F_z(z)$ measurements plotted in the main text and in Fig. S19 have a linear background subtracted, the fitting is performed without subtracting any background and treats the linear background as a fitting parameter. When we apply this fitting method to $\partial_z F_z(z)$ curves on hBN-coupled κ-ET, we implicitly assume the model described in the main text, where the superfluid density is uniform in depth.

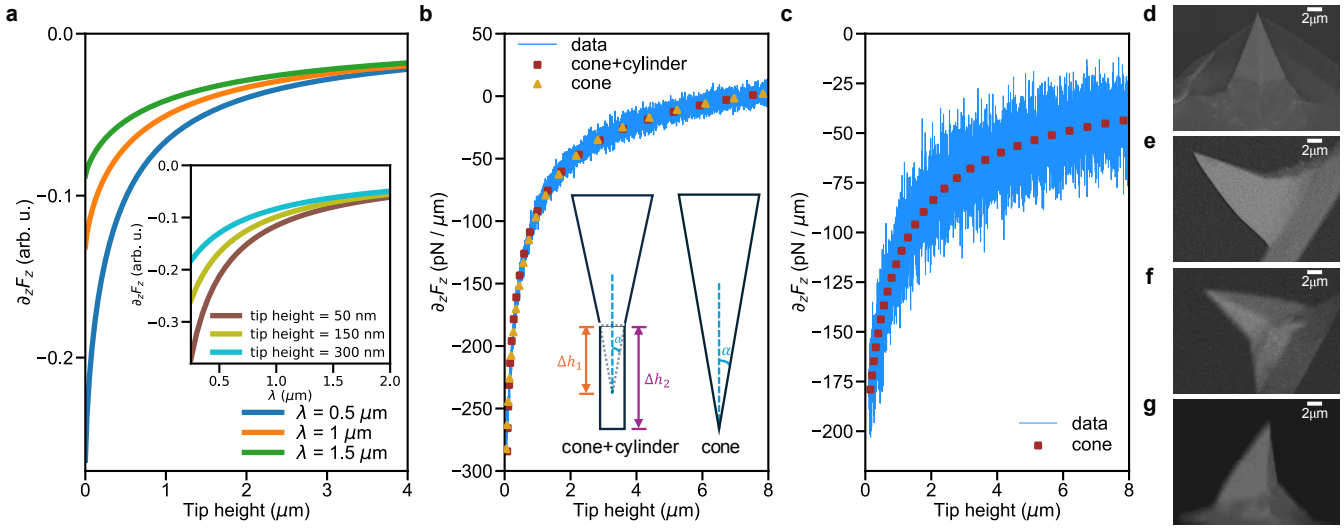

Figure S6: **Modeling the MFM response of a superconductor. a,** $\partial_z F_z$ simulated as a function of tip height for different penetration depths: 0.5 μm (blue), 1 μm (orange), 1.5 μm (green). Inset: $\partial_z F_z$ simulated as a function of penetration depth at different tip heights: 50 nm (brown), 150 nm (olive), 300 nm (cyan). **b,** $\partial_z F_z$ measured as a function of tip height (Device 3) on bare κ-ET (blue), and fitted curves with the cone+cylinder (red) and cone (yellow) model. Fitted parameters are $D = 1800$ pN, $\lambda_{\text{eff}} = 0.691$ μm, $\zeta = 0.00143$ pN $\cdot$ μm^{-2} and $\eta = 11.65$ pN/μm for the cone model and $D = 1800$ pN, $\lambda_{\text{eff}} = 0.680$ μm, $\zeta = 0.00203$ pN $\cdot$ μm^{-2} and $\eta = 6.714$ pN/μm for the cone+cylinder model. Inset: diagrams of the cone+cylinder model and cone model for MFM tips with their defining geometric parameters. **c,** $\partial_z F_z$ measured as a function of tip height (blue) on hBN-coupled κ-ET (Device 4), and fitted curve with the cone model (red). Fitted parameters are $D = 2294$ pN, $\lambda_{\text{eff}} = 1.523$ μm, $\zeta = 0$ and $\eta = -19.43$ pN/μm. **d-g,** SEM images for 4 different MFM tips.

5.3 Converting MFM images to maps of the superconducting penetration depth

Under the assumptions described above, Eq. 28 describes $\partial_z F_z$ as a function of z, λ_{in}, D, ζ, and η. For a given tip on a given region of the sample, D is fixed. So by fitting a $\partial_z F_z(z)$ measurement, we obtain a functional description of $\partial_z F_z$ in terms of the local penetration depth λ_{in}, tip height z, and background η, which enables us to convert constant-height MFM images (fixed z) to maps of the local penetration depth. At fixed z, the linear background term ζz is assimilated into the constant background parameter η, which is determined by comparing the fitted $\partial_z F_z$ curve to the MFM image value over bare κ-ET.

To account for minor inaccuracies in compensating for the tilt of the sample surface, a plane background was subtracted from MFM images, determined over an area of bare κ-ET where superfluid density is uniform. This correction is justified because $\partial_z F_z(z)$ is linear for small variations in z.

5.4 Error analysis

In this section, we estimate the sizes of errors contributing to the local penetration depth extracted from MFM measurements.

5.4.1 Tip geometry

As previously described, we model our MFM tip as a cone or a cone+cylinder (Fig. S6b inset) based on SEM imaging of several tips. The following inaccuracies are associated with this model: (1) the true tip shape differs from the model geometries; (2) angle-dependent parallax and SEM image resolution limit the accuracy of our selection of the tip model parameters; and (3) our model ignores the contributions of the cantilever. We used two models of the sharpest and the bluntest tip geometries that can be justified by the SEM images to estimate that the error in λ_{in} arising from inaccuracy of the tip model is roughly ± 75 nm.

5.4.2 Tip height

In the conversion from MFM images to maps of penetration depth, we assume that the tip moves within a plane of constant height above the κ-ET surface. However, due to imperfect slope compensation and piezo hysteresis, the separation between the tip trajectory and the sample surface deviates from constant within an image.

To quantitatively estimate the effect of imperfect slope compensation, we extract a linear background from a topography image in the region of each MFM image. The slope of the extracted linear background indicates a less than 4% ratio of topographical variation to lateral dimension. Among the MFM images used to extract λ_{in}, the maximum variation of the linear background is around 100 nm. The Meissner force is approximately a function of $\lambda_{\text{in}} + z$ [Luan et al., Phys. Rev. B 81, 100501 (2010)], so errors in tip height translate directly to errors in λ_{in}. However, because we corrected for the surface

tilt using the background subtraction described in Section 5.3, the topographic variations observed serve purely as an upper bound for the resulting error in λ_{in}.

To investigate piezo scanner hysteresis, we look into the difference between forward and backward topography images, measured immediately before each MFM image with similar scanning parameters. We apply a parabolic fit in the fast scanning axis and obtain a maximum variation of 5 nm between forward and backward scans among MFM images, which is negligible compared to other sources of error discussed.

5.4.3 Comparison across devices

Table 2 shows λ_{in} fitted from $\partial_z F_z(z)$ curves measured on bare κ-ET on 3 devices. The uncertainty for each device is obtained from the standard deviation of λ_{in} values from multiple $\partial_z F_z(z)$ measurements on the same device.

Device 1	Device 3	Device 4	Device 5
590 nm ± 100 nm	700 nm ± 130 nm	680 nm ± 70 nm	520 nm ± 10 nm

Table 2: Fitted results of λ_{in} from $\partial_z F_z(z)$ measurements on bare κ-ET from multiple devices at $T = 2$ K. For Device 5, the value and uncertainty of λ_{in} come from the mean and the standard deviation of various fits of a single $\partial_z F_z(z)$ measurement of different ranges from 5 μm to 12 μm.

5.5 Evaluating the superfluid density depth profile

To quantify the size of the suppression of superfluid density observed in hBN/κ-ET, Fig. 4 of the main text employs a simplified model that assumes a uniform superfluid density ρ_{eff} underneath hBN. This model is equivalently framed in terms of a uniform λ_{eff} beneath hBN. The data point of maximal suppression in Fig. 4 of the main text is from the $\partial_z F_z(z)$ data with the fitting method shown in Fig. S6, and gives $\rho_{\text{eff}}/\rho_0 \approx 25\%$ or equivalently $\lambda_{\text{eff}} \approx 2\lambda_0$. This simple model fits the $\partial_z F_z(z)$ data well, but is physically unrealistic as we expect the suppression to be strongest near the hBN/κ-ET interface and to decay into the bulk. In this section, we show that the simple model from Fig. 4 of the main text deviates only slightly from a more realistic model with a spatial decay of the superfluid density.

To that end, we solve Eq. (18) using a modified penetration depth that assumes an exponential decay within the superconductor:

$$\lambda_{\text{in}}(z) = \lambda_0 / \left(1 - \alpha e^{z/z_0}\right) \tag{29}$$

Two parameters control the spatial variation of λ_{in}: z_0, which sets the decay length, and α, which determines the surface value. We use a single magnetic dipole in place of the full tip geometry.

The computational details are as follows: To numerically solve Eq. (18) with the z-dependent penetration depth in Eq. (29), we adopt the finite element method with a two-domain computational scheme [Gulian, Shortcut to Superconductivity (Springer, 2020); Oripov and Anlage, Phys. Rev. E 101, 033306 (2020)]. The simulation domain is divided into superconducting and vacuum regions, modeled as two concentric coaxial cylinders. The radius and height of the superconducting domain are $(r_0, h_0) = (8\lambda_0, 8\lambda_0)$ and those of the vacuum domain are $(R_0, H_0) = (2r_0, 3h_0)$, respectively. The common axis is aligned with the $\hat{\boldsymbol{z}}$ direction, and the upper surface of the superconducting domain is located at $z = 0$ in the cylindrical coordinate system. We assign the upper and lower parts of Eq. (18), with the dipole vector potential given in Eq. (20), to the superconducting and vacuum domains:

$$\nabla^2 \mathbf{A} = \begin{cases} \mathbf{A}/\lambda_{\text{in}}^2 & \Omega_{\text{sc}} \\ \nabla^2 \mathbf{A}_{\text{dip}} & \Omega_{\text{va}} \end{cases} \tag{30}$$

where Ω_{sc} and Ω_{va} denote the superconducting and vacuum domains, respectively, as defined above. We solve Eq. (30) using the finite element analysis implemented in COMSOL Multiphysics. Since the magnetic field far from the superconductor should match that of a magnetic dipole in vacuum, we impose $\boldsymbol{A} = \boldsymbol{A}_{\text{dip}}$ at the outer boundary of the vacuum domain as a boundary condition. From the resulting vector potential $\boldsymbol{A}$, we extract the induced Meissner magnetic field $\boldsymbol{B}_{\text{ind}} = \nabla \times \boldsymbol{A}_{\text{ind}} = \nabla \times (\boldsymbol{A} - \boldsymbol{A}_{\text{dip}})$. Representative results are shown in Fig. S7.

6 $\partial_z F_z$ measurements on hBN/BSCCO

Measurements of $\partial_z F_z(z)$ on thin and finite-sized samples of BSCCO showed background forces larger than those on the bulk κ-ET crystals. These background forces were empirically uniform within the measurement region, and probably result from the electrostatic environment of the insulating SiO_2 substrate. In order to extract the Meissner force from the $\partial_z F_z(z)$ measurement, we subtracted the $\partial_z F_z(z)$ measurement taken over bare SiO_2 from the measurements taken on the BSCCO heterostructure, as shown in Fig. S8d. Spatial variations in the Meissner force are apparent when moving to the flake edge, but no significant variations are attributable to encapsulation with hBN, as shown by the measurements moving from bare BSCCO onto hBN/BSCCO in Fig. S8e.

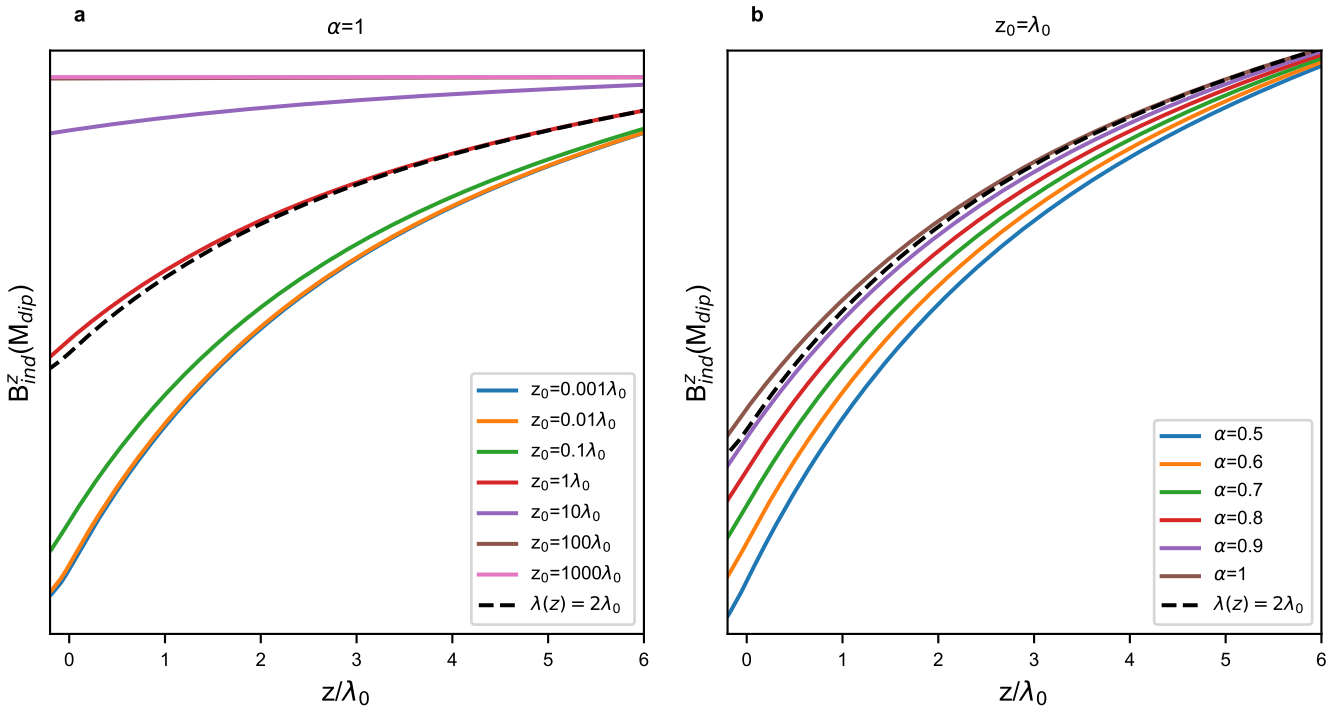

Figure S7: **Meissner response with non-uniform superfluid density profile.** $z-$component of the induced magnetic field, $B^z_{\rm ind} = \boldsymbol{B}_{\rm ind} \cdot \hat{\boldsymbol{z}}$ as a function of z. **a,** Comparison between the constant $\lambda_{\rm in} = 2\lambda_0$ case and several values of z_0, with $\alpha = 1$ fixed in Eq. 29. **b,** Comparison between $\lambda_{\rm in} = 2\lambda_0$ case and several values of α, with $z_0 = 1$ fixed. The magnetic dipole is located at $a = 6\lambda_0$, and $M_{\rm dip} \equiv \mu_0 m/(4\pi\lambda_0^2)$.

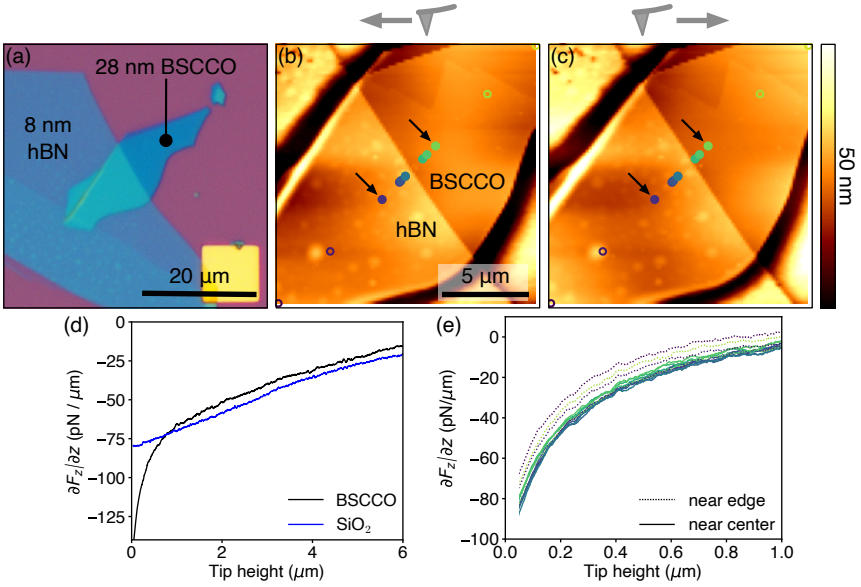

Figure S8: **Meissner force in proximity to an hBN/BSCCO interface**. **a,** Optical image of sample with a 28-nm flake of BSCCO OD55K partially encapsulated by an 8-nm flake of hBN. **b, c,** Topographic images of the sample taken at $T = 2.0$ K with locations of $\partial_z F_z(z)$ curves overlaid. Open circles are points far from the flake center. Images from the forward and backward scans are shown to indicate the uncertainty in the curve locations. The black arrows indicate the curves presented in the main text. Line-by-line linear background subtraction applied. **d,** $\partial_z F_z(z)$ measured on bare BSCCO and bare SiO_2. Multiple individual measurements taken at each location were averaged, then the data was smoothed with a uniform filter with 30-50-nm width. **e,** $\partial_z F_z(z)$ measured on hBN/BSCCO and on bare BSCCO, with the SiO_2 spectrum subtracted. Dotted lines are for the locations far from the flake center (open circles in b, c). The curves have been aligned in z so that the BSCCO surface is at the same z for all.

7 Evaluating electrostatic forces in MFM experiments

In this section, we quantify the contribution of electrostatic forces to the total $\partial_z F_z$ measured by MFM. Locally, the different materials' work functions introduce a spatially varying force on the tip, as the local contact potential difference (CPD) creates an electric field between the tip and the sample. The MFM images in Fig. 2b and c of the main text were taken with a constant tip bias chosen to offset the CPD over hBN/κ-ET. Therefore, an electrostatic force is expected to be present over other regions. To understand these variations, we first used sideband Kelvin probe force microscopy (KPFM) to image the local CPD. In KPFM, a feedback loop adjusts the tip bias to correct for the local CPD continuously while scanning [Nonnenmacher et al., Appl. Phys. Lett. 58, 2921 (1991)]. Fig. S9a and b show the simultaneously recorded topography and KPFM in a slightly larger field of view than in Fig. 2b and c of the main text. hBN/κ-ET, bare κ-ET, and $RuCl_3$/κ-ET are all present within the frame. KPFM shows variation in the local CPD, especially over $RuCl_3$, but the CPD never exceeds $\pm$200 mV.

To evaluate the importance of these CPD variations, we measured $\partial_z F_z$ as a function of tip bias at four different locations (markers in panel b), with the tip lifted 150 nm above the κ-ET surface (Fig. S9d). These curves are dominated by a parabolic shape, and the tip bias that compensates for the CPD is at the minimum of the parabola, where the electrostatic force is minimized. To isolate the electrostatic contribution, we have subtracted the minimum value of $\partial_z F_z$, so that we present $\partial_z F_z^{\mathrm{El}}(V_{\mathrm{tip}}) = \partial_z F_z(V_{\mathrm{tip}}) - \partial_z F_z(V_{\mathrm{CPD}})$, where V_{tip} is the tip bias and V_{CPD} is the CPD. At the tip bias used for MFM imaging (95 mV, vertical dashed line), $\partial_z F_z^{\mathrm{El}}$ is much less than 5 pN/μm at all four locations. The tip-bias curves were measured with the tip closer to the sample surface than it was for the MFM image. So at the MFM imaging height, the electrostatic force gradient would be even weaker, making electrostatic artifacts insignificant compared to the roughly 40 pN/μm variation seen in the MFM image in panel c.

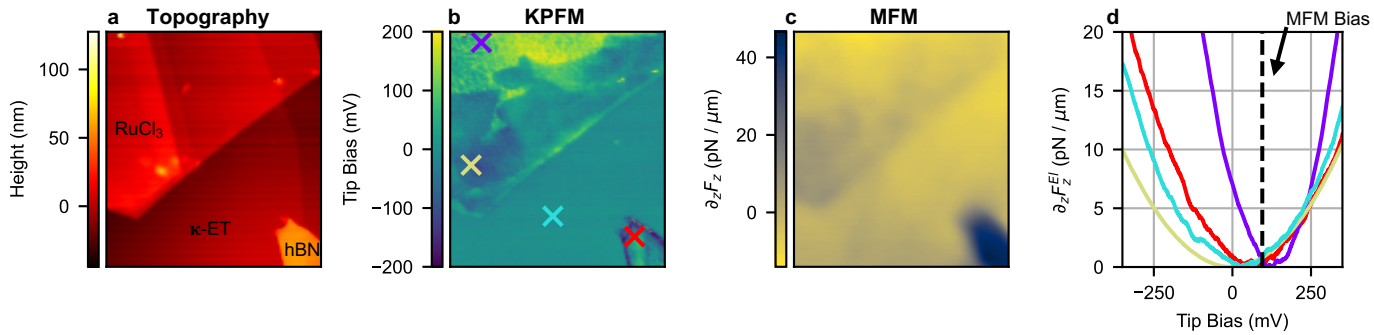

Figure S9: **Quantifying electrostatic forces in MFM experiments**. **a, b,** Topography and simultaneously recorded KPFM on Device 1 in a region including hBN/κ-ET, $RuCl_3$/κ-ET, and bare κ-ET. The region is the same as the region shown in Fig. 2 of the main text but with a larger field of view. The tip bias modulation applied for KPFM was 550 Hz and 1 V amplitude. **c,** Constant-height MFM in the same field of view (tip height 300 nm above κ-ET, tip bias 95mV). This is the same data shown in Fig. 3b, but cropped to a larger frame. **d,** $\partial_z F_z^{El}$, the electrostatic contribution to the force gradient, measured as a function of tip bias. Tip height is 150 nm above the κ-ET surface. The tip bias used for MFM is marked by the vertical line.

8 Interface inhomogeneities

The hBN/κ-ET devices show a spatial inhomogeneity in the suppression of superfluid density. In Fig. 3 in the main text, we compile the maximally suppressed values. In all devices, we observe wrinkles in the hBN at low temperature, providing a spatially varying character of the interface with κ-ET. We focus on a representative 8×8 μm^2 region of Device 3 that has wrinkles separated by lateral spacings on the order of 5 μm (topography in Fig. S10a). At 2 K, imaging $\partial_z F_z$ 95 nm above the κ-ET surface (Fig. S10b) shows uniform $\partial_z F_z$ over bare κ-ET but strong variation over the hBN/κ-ET. Over the flat areas of hBN, $\partial_z F_z$ is suppressed. However, near the wrinkles, $\partial_z F_z$ is indistinguishable from that of bare κ-ET. The contrast between the flat and wrinkled areas, roughly 30 pN/μm at 2 K, dissipates with increasing temperature (MFM and topography profiles in Fig. S10c and d, where the height in d is with respect to the hBN surface). Near 10 K, slightly below the critical temperature T_c, the contrast falls below the measurement noise (red line in c). Note that the contrast may become small just below T_c because: (1) the weakened forces associated with the large λ near T_c will reduce the scale of modulations (panel c), and (2) the increased depth probed by the Meissner force with the large λ will further decrease the sensitivity to the region impacted by hBN.

These observations indicate that the impact of hBN on the superfluid density is impeded by the morphological changes near the wrinkles, which are possibly associated with the hBN crystal orientation or strain. Interestingly, broader lumps in the topography, probably indicating bubbles between the hBN and κ-ET (with a height of 10nm) have a much weaker, nearly imperceptible, impact on the superfluid density (white arrow in panels a and b), suggesting that the coupling is unimpeded by nanoscale spacings between hBN and κ-ET. In Fig S10c, we present constant-height MFM line cuts at 2 K, 5 K, and 10

K. The corresponding constant-height MFM images are presented in Fig S11.

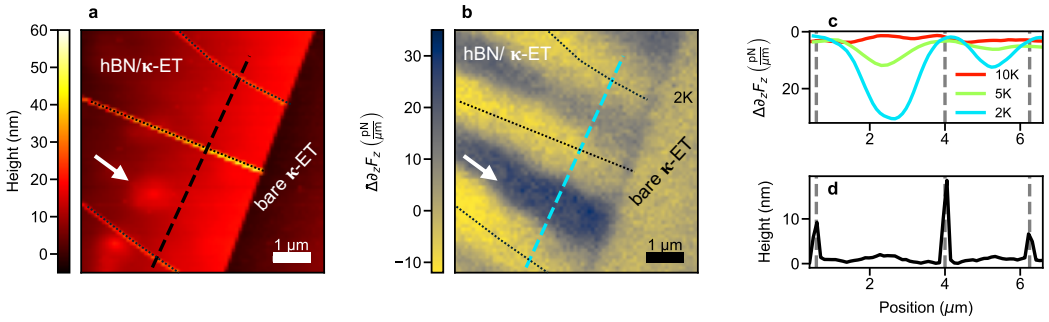

Figure S10: **Variations in hBN geometry.** **a,** Topographic image of the hBN flake on top of the bulk κ-ET crystal surface at $T = 2$ K (Device 3). Black dotted lines mark sharp wrinkles in the hBN. The white arrow marks a smooth bubble. **b,** Constant-height MFM showing suppressed $\partial_z F_z$ between the wrinkles (black dashed lines). The tip was lifted 75 nm above the hBN surface. The value of $\partial_z F_z$ over bare κ-ET is subtracted from the entire image. The dashed lines in a and b mark the locations of the profiles shown in c and d. **c,** Profiles from constant-height MFM images measured at 2 K, 5 K, and 10 K, showing that the feature contrast disappears on heating to T_c. **d,** Topographic profile at the same location as the MFM in c, showing that the hBN wrinkles are aligned with the regions of unaltered superconductivity ($\Delta\partial_z F_z = 0$).

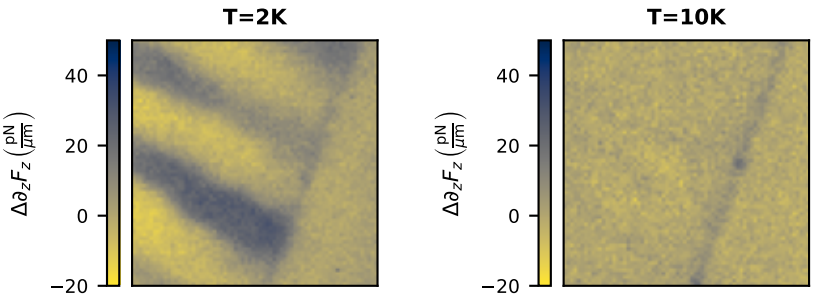

Figure S11: **Temperature-dependence of MFM with spatially varying hBN geometry.** Constant-height MFM scans at 75-nm lift height at 2 K and 10 K (Device 3). At 10 K, the contrast is below our measurement noise. The scans share color scales.

As seen in Figs. S10,S11, the suppression of superfluid density can display spatial inhomogeneity under hBN. In Fig. S12 a-c, we show large-area constant-height MFM on three different devices, all displaying spatial inhomogeneity. Fig. S12 d-f display the corresponding topography images, with hBN wrinkles highlighted by black dotted lines. The dotted light blue lines in b and e mark a step edge in hBN. In all devices, the suppression is consistently recovered between the hBN wrinkles.

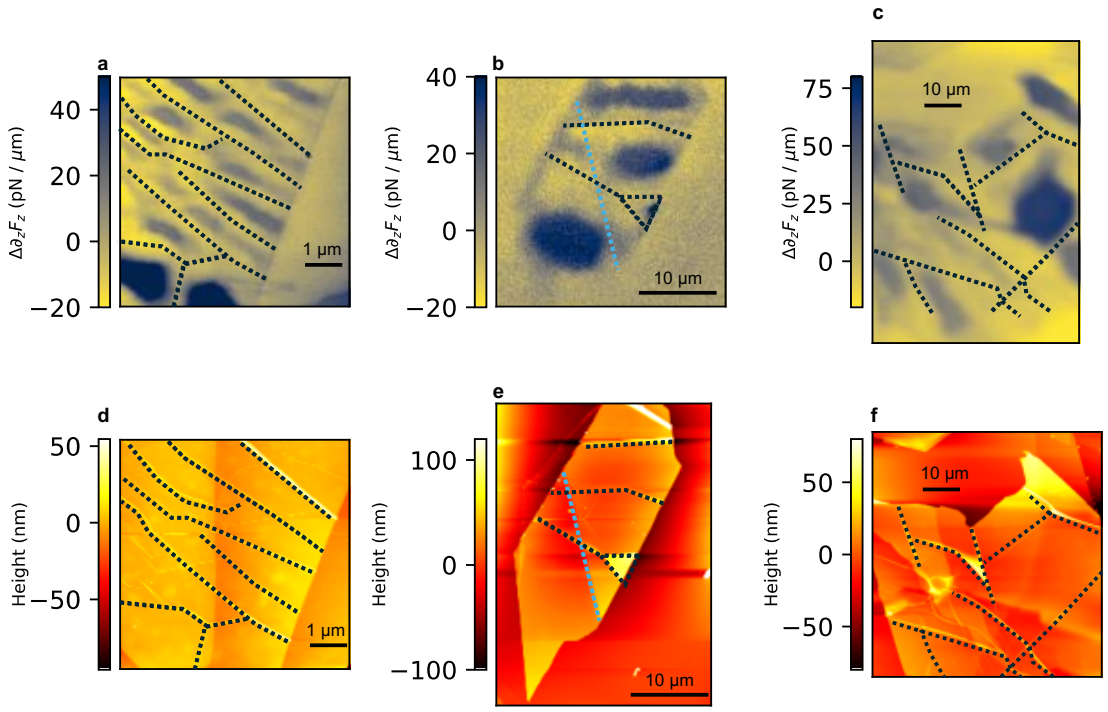

Figure S12: **Meissner effect in structures with hBN "wrinkles". a-c,** Constant-height MFM on 3 devices. Tip lift heights are 95 nm (a , Device 3) 150 nm (b, Device 4), and 300 nm (c, Device 1). **d-f,** Topography images corresponding to the MFM images. Dotted black lines indicate wrinkles in the hBN. Dotted blue lines indicate a step in the hBN thickness.

In Fig. S13a we display a zoomed-out MFM scan of Fig. 2b in the main text (panel b depicts the corresponding topography image). Across a large scan area, the effect of $RuCl_3$ on κ-ET is reproducibly weak compared to the hBN/κ-ET interface (bottom right corner in panel a). Interestingly, $\sim$ 5-nm steps in κ-ET topography do not appear in constant-height MFM. The change in κ-ET surface height of such steps can be interpreted as layers of κ-ET where superconductivity is fully suppressed. This observation establishes a lower bound on the depth of the affected κ-ET layer. Furthermore, from this observation, we conclude that suppression of superfluid density over a depth of only a few nanometers results in a change to $\partial_z F_z$ below our measurement noise. In Fig. S13c,d we present constant-height MFM over the $RuCl_3$/κ-ET interface of Device 5. Here, the weak effect of $RuCl_3$ on κ-ET is reproduced.

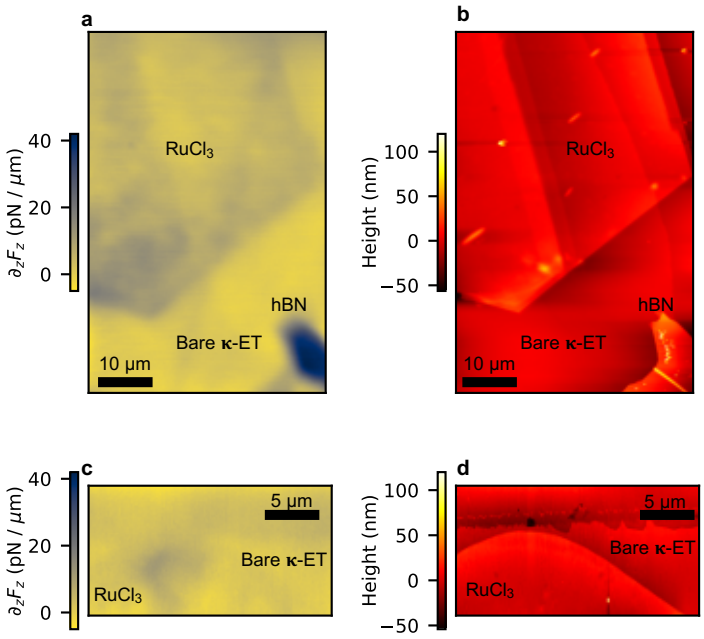

Figure S13: **Large-scale images of $RuCl_3$/κ-ET structures. a,** Constant-height MFM (lift=150 nm) above the $RuCl_3$/κ-ET and hBN/κ-ET interfaces of Device 1. The dominant signal originates from the hBN/κ-ET interface. $RuCl_3$ shows significantly weaker suppression over a large scale. By contrast, hBN crystals have shown significant suppression of superfluid density over similar length scales. **b,** Topography image corresponding to the MFM image. **c,** Constant-height MFM (lift=300 nm) above the $RuCl_3$/κ-ET interface of Device 5. The color scale is shared with a. **d,** Topography corresponding to c.

9 Estimating the depth profile of the superfluid density suppression in hBN/κ-ET heterostructures

To estimate a lower bound on the depth of suppressed superconductivity within the κ-ET crystal, we consider a simplified model in which superconductivity is completely absent within a surface layer of thickness D under the hBN/κ-ET interface. This differs from the model in the main text, where superconductivity is assumed to be modified beneath the hBN layer while remaining homogeneous throughout the depth of the crystal. We describe this model in Fig. S14a. The scenario in which a tip hovers at height z over a superconductor with a fully suppressed layer of thickness D is equivalent to a scenario with a tip lifted to a height of $z + D$ above an unaffected superconductor. In Fig. S14b, we schematically draw a more realistic picture, in which the superfluid density smoothly transitions to the bulk value ρ_0 over a characteristic length D*. To achieve equal repulsive forces on the tip in the scenarios in a and b, D* must satisfy $D^* > D$, making D a lower bound for the thickness of the affected layer. In Fig. S14c, we present the two measurements from Fig. 1a. The red line shows the z-shift needed to overlay the curves. In Fig. S14d, we shift the hBN/κ-ET curve to the left by 430 nm (dotted blue curve). The bare ET and shifted hBN/κ-ET curves are in good agreement. It is important to note that the estimate of complete suppression is on the order of a few hundred nanometers, matching the phonon polariton wavelengths.

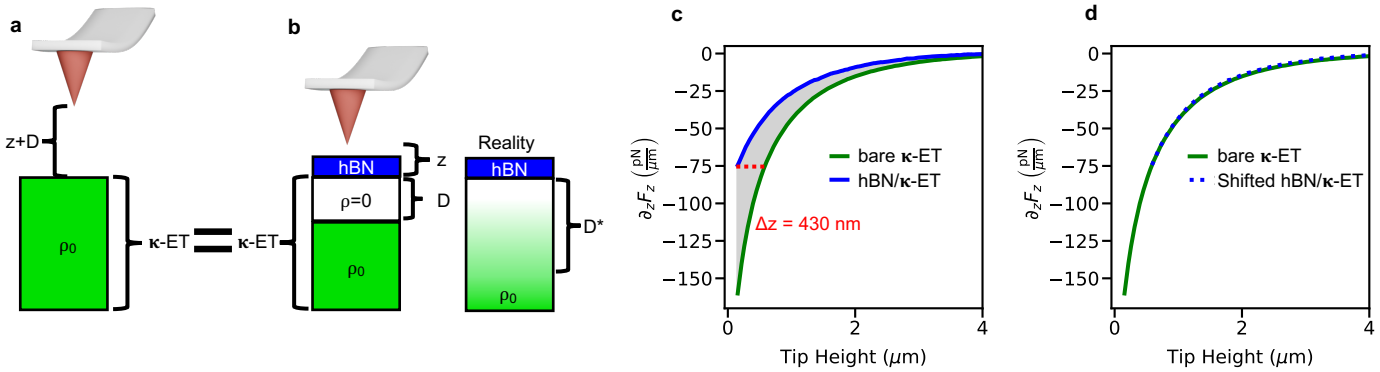

Figure S14: **Evaluating the depth profile of the suppression of superfluid density**. **a,** Schematic for the fully suppressed superconductivity model. A tip hovering at height z above a superconductor with a fully suppressed layer of depth D, is equivalent to a tip hovering at height $z + D$ above an unaffected superconductor. **b,** Schematic of the realistic distribution of superfluid density inside a suppressed superconductor. **c,** The two $\partial_z F_z(z)$ measurements on hBN/κ-ET (blue) and bare κ-ET (green) from the main text. **d,** Same as a, except the hBN/κ-ET curve is shifted to the right by 430 nm (dotted blue curve).

10 Quantifying mode coupling strength at the hBN/κ-ET interface

10.1 Eigenmodes of the coupled system

We use the transfer matrix approach for the calculation of the HPhP eigenmodes. Although the maximum of Im r_p is a good indicator for the position of poles at low dissipation, such an approximation fails in material systems with high losses [Ruta et al., Nat. Commun. 14, 8261 (2023)]. We therefore calculate the poles by numerically evaluating $\frac{1}{\mathrm{Abs}(r_p)} = 0$, where r_p is the Fresnel reflection coefficient for p-polarized light [Bylinkin et al., Nat. Photon. 15, 197 (2021)]. Two types of eigenmodes–spatially decaying eigenmodes and temporally decaying eigenmodes – can be calculated. These two types arise from the fact that the dissipation of a wave can be represented through either complex momentum or complex frequency, but not both (i.e., $e^{i[(q+i\kappa)x-\omega t]} = e^{i[qx-(\omega-i\gamma)t]}$). For spatially decaying modes, we consider complex momenta $q + i\kappa$ and real frequencies ω, which represent waves decaying spatially with propagation length $L_{pp} = 1/\kappa$. For temporally decaying modes, we consider real momenta q and complex frequencies $\omega - i\gamma$, which represent waves decaying temporally with lifetime $\tau = 1/\gamma$. The poles for $r_p(q + i\kappa, \omega)$ and $r_p(q, \omega - i\gamma)$ are shown in red and blue in Fig. S15 against Im r_p calculated for real momenta and frequencies.

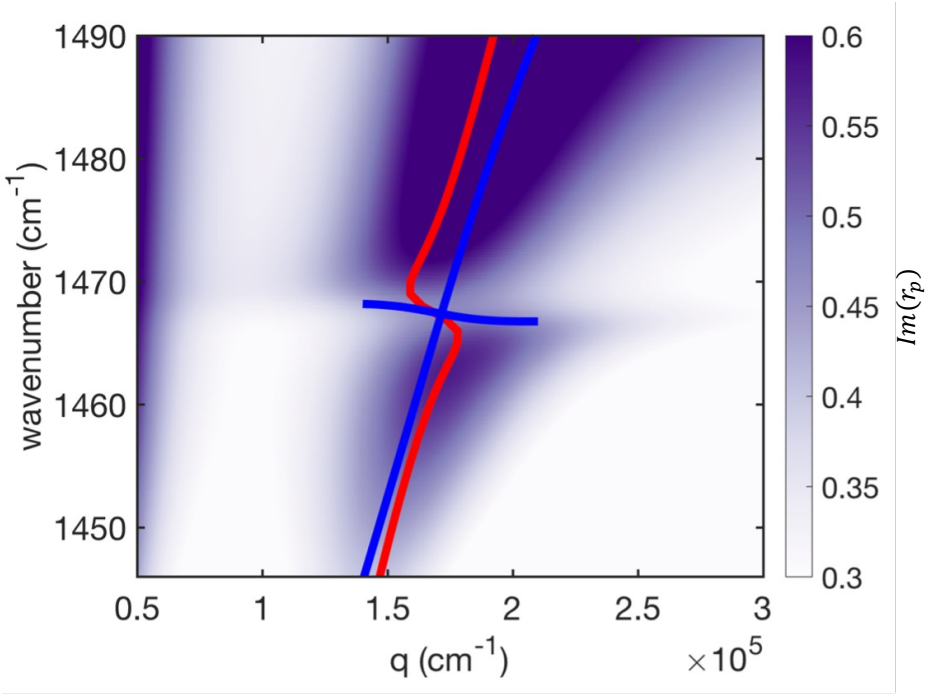

Figure S15: **HPhP dispersion in hBN/κ-ET**. Calculated spatially (red) and temporally (blue) decaying eigenmodes overlaid on Im r_p.

No anti-crossing is observed in the temporally decaying eigenmodes, indicating weak coupling between the propagating phonon polaritons in hBN and κ-ET. We deepen our insights into the coupling condition by hypothetically varying the oscillator strength of κ-ET and observing the shift in the coupling regime. The coupling between hBN and κ-ET can be modeled as that between two damped coupled harmonic oscillators. This open quantum system can be described by a non-Hermitian Hamiltonian with complex frequencies $\tilde{\omega}_j$ $(j = 1, 2)$ along the diagonal and coupling constant g in the off-diagonal elements. The eigenvalues of the Hamiltonian are solved to be $\omega_\pm = \tilde{\omega}_{\mathrm{ave}} \pm \frac{\tilde{\Delta}}{2}\sqrt{1 + \left(\frac{2g}{\tilde{\Delta}}\right)^2}$, where $\tilde{\omega}_{\mathrm{ave}} = (\tilde{\omega}_1 + \tilde{\omega}_2)/2$ is the average complex frequency and $\tilde{\Delta} = \tilde{\omega}_1 - \tilde{\omega}_2$ is the complex detuning [Peters and Rodriguez, Phys. Rev. Lett. 129, 013901 (2022); Rodriguez, Eur. J. Phys. 37, 025802 (2016)]. Denoting ω_+ and ω_- as $\omega_1 - i\gamma_1$ and $\omega_2 - i\gamma_2$, respectively, it can be realized that $\omega_1 \neq \omega_2, \gamma_1 = \gamma_2$ for $g \gg 1$ and $\omega_1 = \omega_2, \gamma_1 \neq \gamma_2$ for $g \ll 1$. We choose $\omega_1 \neq \omega_2, \gamma_1 = \gamma_2$ and $\omega_1 = \omega_2, \gamma_1 \neq \gamma_2$ as the conditions for strong and weak coupling, respectively.

As shown in Fig. S16a and Fig. S16b, the transition from weak to strong coupling occurs at an increase of approximately 4.5 times the κ-ET oscillator strength, i.e. $s_{\mathrm{new}} = s_0 + 4.5s_0$, where s_{new} and s_0 are the increased and original oscillator strengths. The difference between γ_1 and γ_2 gradually decreases until a split appears between ω_1 and ω_2. Examples of poles under the weak and strong coupling regimes are shown in Fig. S16c and Fig. S16d respectively. The coupling between the hBN phonon-polaritons and κ-ET is far from the strong coupling regime.

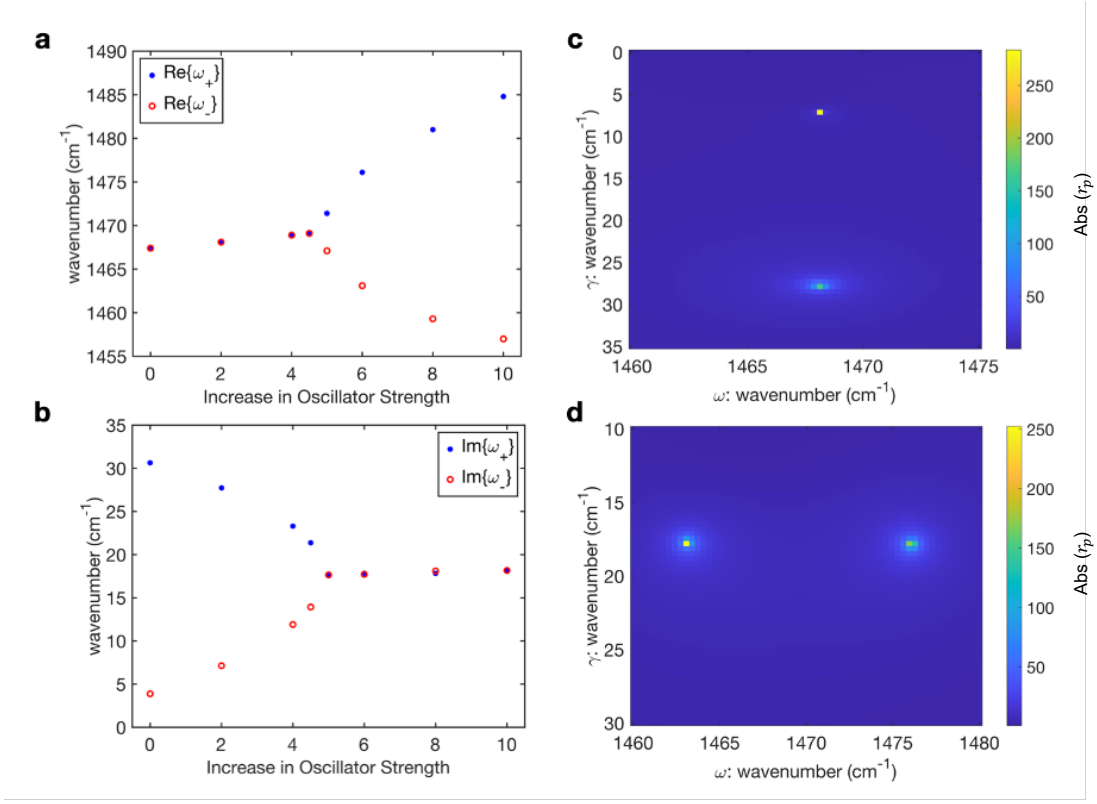

Figure S16: **Eigenvalues and coupling regimes. a,b,** The poles ω_+, ω_- as functions of the increase in oscillator strength for κ-ET. An increase of 0 indicates no change to the oscillator strength of κ-ET. The real and imaginary parts of the poles are shown in the top and bottom figures respectively. **c,** Poles under the weak coupling regime (2x increase). **d,** Poles under the strong coupling regime (6x increase).

10.2 Simulation of the real-space s-SNOM experiment

We now relate the obstruction in the dispersion relation theoretically predicted in Fig. 4a of the main text to the kink experimentally observed in the real space s-SNOM in Fig. 4c. The s-SNOM fringes are the standing wave pattern produced by the interference of propagating polaritons. Each fringe is impacted by the interaction between the HPhPs and the C=C stretching mode. This impact manifests as a change in the HPhP wavelength compared to the non-interacting case. If we denote the wavelength change as $\delta\lambda$, then after n oscillation periods, the total travel length difference is $n\delta\lambda$. Therefore, the shift in the interference fringes is cumulative and larger for higher-order fringes.

We demonstrate this effect concretely with theoretical simulations. We first calculate the HPhP dispersions for 32-nm-thick hBN on 280-nm-thick SiO_2/Si (Fig. S17a) and for 32-nm-thick hBN on 100-nm-thick κ-ET (Fig. S17b; identical to Fig. 4a in the main text). Notably, the obstruction in the dispersion observed in the hBN/κ-ET case is absent in the hBN/SiO_2 system (blue box in panels a,b). Using these dispersions, we then simulate the real-space interference patterns measured by s-SNOM, obtaining the nano-IR scattering amplitude maps shown in Fig. S17c (hBN/SiO_2) and Fig. S17d (hBN/κ-ET). These maps are calculated using the equation

$$\zeta(x) = A\frac{-2x}{L_p}\frac{\sin\left(4\pi\frac{x-x_A}{\lambda_p}\right)}{\sqrt{x}} + B\frac{-x}{L_p}\frac{\sin\left(2\pi\frac{x-x_B}{\lambda_p}\right)}{x}$$

where L_p and λ_p are the propagation lengths and wavelengths, respectively, of the spatially decaying modes obtained from the eigenmode calculation (as described in the previous subsection). The first and second terms correspond to the tip-launched and edge-launched components. The tip-launched component originates from the tip and reflects back from the straight edge, traveling a total distance of $2x$. On the other hand, the edge-launched component originates from the edge and travels a distance x to be detected by the tip. The amplitudes and shifts of these components are represented by A/B and x_A/x_B, respectively. The denominators of the two terms are determined by the geometry of the experimental setup. For the simulation, the ratio $A:B$ is set to $1:10$, so that the edge-launched component dominates, as observed in the experimental data.

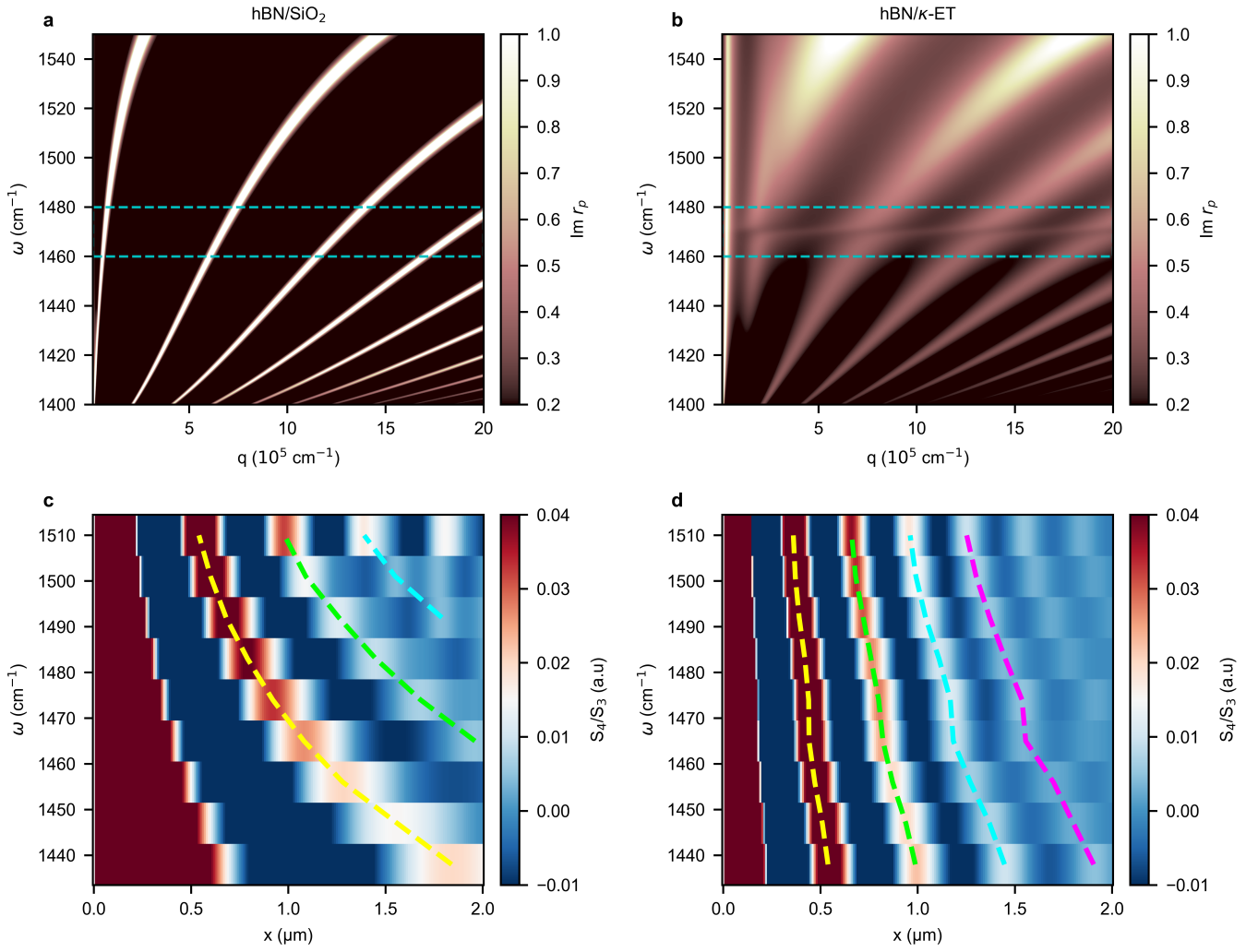

Figure S17: **Polaritonic dispersion and mode hybridization in hBN/κ-ET structures. a,b,** Phonon-polariton dispersion for the (a) hBN/SiO_2 (32-nm hBN, 280-nm SiO_2) and (b) hBN/κ-ET (32-nm hBN, 100-nm κ-ET) interfaces, represented by false color maps of the imaginary part of the Fresnel reflection coefficient r_p. **c,d,** The corresponding simulated hyperspectral images of S_4/S_3. Kinks in the dispersion and real-space s-SNOM simulations in the hBN/κ-ET case are a consequence of coupling.

11 Molecular Langevin dynamics

In this section, we provide calculation details for the molecular Langevin dynamics simulations used to investigate the interaction between the C=C stretching mode of κ-ET and the electric field induced by the hBN HMs. The effective potential of the C=C stretching mode and the E_{2g} (in-plane TO) modes of hBN were obtained from density functional theory (DFT) calculations using the Vienna Ab initio Simulation Package [Kresse and Joubert, Phys. Rev. B 59, 1758 (1999)]. We used the Perdew-Burke-Ernzerhof [Perdew et al., Phys. Rev. Lett. 77, 3865 (1996)] exchange-correlation functional for the description of electron-electron exchange and correlation and the DFT+D3BJ functional for van der Waals interaction. We restricted the Brillouin zone sampling to the gamma-point and employed a plane wave energy cut-off of 400 eV. We considered a 6×4 rectangular bilayer of hBN (96 Boron and 96 Nitrogen atoms) separated from a BEDT-TTF dimer with van der Waals distance 3 Å; the vacuum layer is described as a 20-Å out-of-plane space under the three-dimensional periodic boundary conditions. Since the BEDT-TTF dimer exists as a +1 charged state, we applied the +1 charge condition in this calculation. We evaluated the potential energy surface of the C=C stretching mode of κ-ET ($V_{\mathrm{CC}}(Q_{\mathrm{CC}})$) and the E_{2g} phonon modes of hBN ($V_{\mathrm{hBN}}(Q_{\mathrm{hBN}})$). In addition, we evaluated the induced dipole moment of the C=C stretching mode with lattice distortions along the mode eigenvector to obtain the mode effective charge ($Z_{\mathrm{CC}} = 7.7e$). Based on these first-principle calculations, we then set up a Langevin equation at $T = 4$ K, with η representing white noise and $\gamma = 2$ THz, as follows:

$$m_{\mathrm{CC}}\,\ddot{Q}_{\mathrm{CC}}(t) = -\frac{\partial V_{\mathrm{CC}}}{\partial Q_{\mathrm{CC}}} - \gamma\,\dot{Q}_{\mathrm{CC}}(t) + \sqrt{2\,k_B T\,\gamma}\;\eta_{\mathrm{CC}}(t) - \frac{\partial (V_{\mathrm{HM}} + V_{\mathrm{CC-hBN}})}{\partial Q_{\mathrm{CC}}}$$

$$m_{\mathrm{hBN}}\,\ddot{Q}_{\mathrm{hBN}}(t) = -\frac{\partial V_{\mathrm{hBN}}}{\partial Q_{\mathrm{hBN}}} - \gamma\,\dot{Q}_{\mathrm{hBN}}(t) + \sqrt{2\,k_B T\,\gamma}\;\eta_{\mathrm{hBN}}(t) - \frac{\partial (V_{\mathrm{HM}} + V_{\mathrm{CC-hBN}})}{\partial Q_{\mathrm{hBN}}}$$

Here, $V_{\mathrm{HM}}[Q_{\mathrm{CC}}, Q_{\mathrm{hBN}}] = Z_{\mathrm{CC}} Q_{\mathrm{CC}} E^z_{\mathrm{HM}}[Q_{\mathrm{hBN}}]$ is the coupling between the dipole of the C=C stretching mode and the out-of-plane field induced by the hBN HM, and $V_{\mathrm{CC-hBN}}[Q_{\mathrm{CC}}, Q_{\mathrm{hBN}}]$ is the phonon-phonon scattering interaction evaluated by density functional theory calculations. All parameters for the effective potentials were obtained from the DFT calculations described above. However, the relation between the out-of-plane electric field (E^z_{HM}) and displacement along Q_{hBN} remains undetermined, so as a rough estimate, we implemented a linear relation: $E^z_{\mathrm{HM}}[Q_{\mathrm{hBN}}] = f_{\mathrm{HM}} Q_{\mathrm{hBN}}$. With a given factor f_{HM}, the time-averaged electric field ($E_{avg} = \frac{1}{T}\int_0^T dt |E^z_{\mathrm{HM}}[Q_{\mathrm{hBN}}(t)]|$) was used to determine the field strength. With the above assumptions, the Langevin dynamics evolved stably, and the averaged temperature (kinetic energy) for each oscillator was 2 K. While the frequencies of the E_{2g} and C=C modes at $q = 0$ were determined by the polynomial potentials obtained from DFT calculations, we manually adjusted the mass of the hBN mode to tune the HM frequency into resonance with the C=C mode. The Fourier spectrum of the electric field induced by the HM mode ($E^z_{\mathrm{HM}}[Q_{\mathrm{hBN}}(t)]$) is shown in Fig. S18. The Langevin dynamics broaden the HM mode such that the electric field spectrum covers the range of hyperbolicity in hBN, as well as the C=C mode frequency.

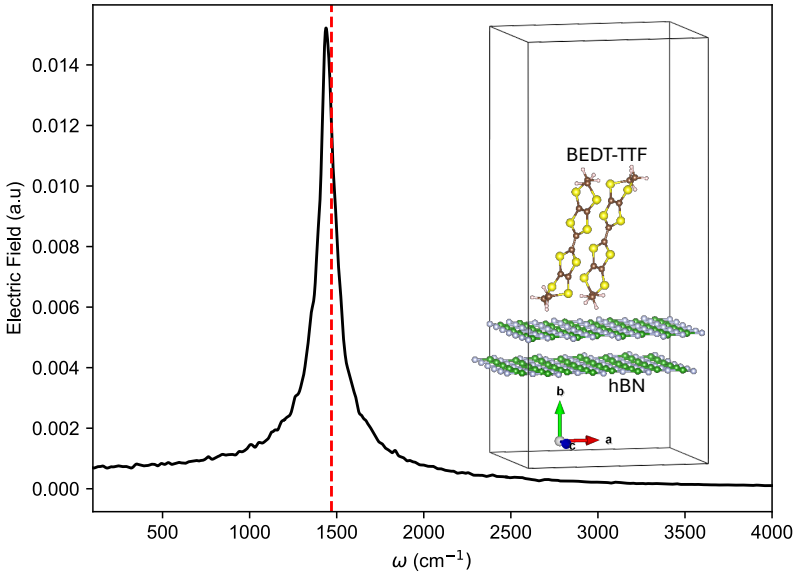

Figure S18: **Electric field simulating the HM evanescent field.** The red vertical line marks the C=C mode frequency.

12 Reproducibility of the Meissner force across devices

12.1 Bare κ-ET

In Fig. 2a in the main text, we present measurements of temperature-dependent $\partial_z F_z(z)$ on bare κ-ET taken on Device 6. Measurements on 5 different devices (Fig. S19) show behavior that is characteristic of the Meissner effect: a strong nonlinear repulsive force that develops below T_c. A small slope is noticeable at T_c and is attributable to background forces impacted by the tip cleanliness and helium exchange gas. For all samples, locating the device requires extensive topographic scanning, which inevitably introduces some material on the tip; the helium exchange gas is required to achieve low temperatures using our MFM instrument.

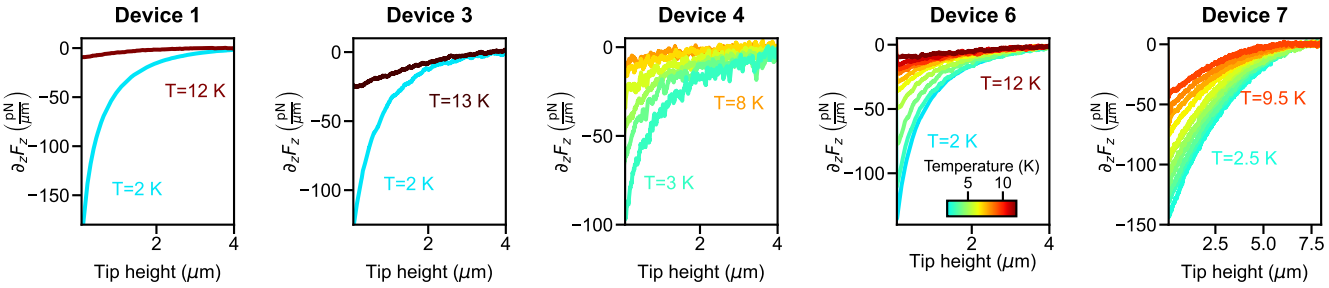

Figure S19: **$\partial_z F_z(z)$ for bare κ-ET crystals at varying temperatures.** $\partial_z F_z(z)$ for 5 different devices on bare κ-ET. For Devices 1, 3, and 4, $\partial_z F_z(z)$ was measured separately at different temperatures. For Devices 6 and 7, $\partial_z F_z(z)$ was measured while continuously ramping the temperature. In this case, we used a linear-in-temperature calibration to approximate the temperature dependence of the piezo-response in the AFM scanners. Note that Device 7 is an additional bare κ-ET crystal, with a cleaved surface, that does not contribute to the data shown in the main text.

12.2 hBN/κ-ET

Representative temperature-dependent $\partial_z F_z(z)$ data for hBN/κ-ET (Device 3) are presented in Fig. S20. Here, to accurately measure above the same location across temperatures, we employ tapping mode scanning to correct for piezo drifts, which occur when the temperature changes. In this process, as mentioned above, the tip cleanliness is compromised. This experimental aspect introduces additional uncertainties into the extraction of the absolute values of the superfluid density, especially near T_c. For this reason, power-law dependences of the superfluid density at the hBN/κ-ET interface were not analyzed.

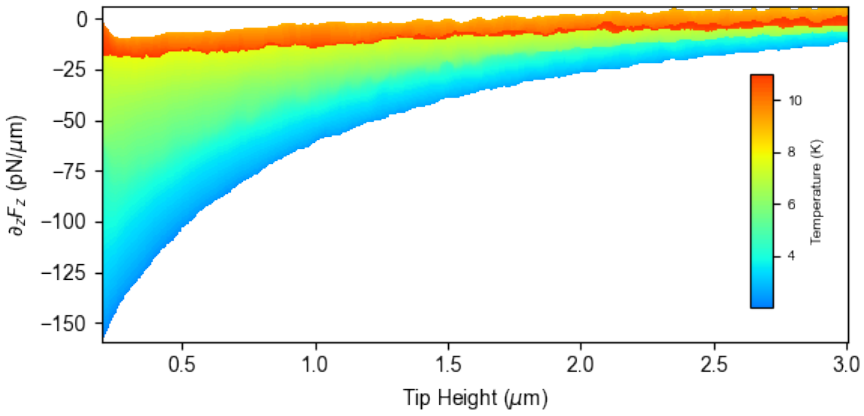

Figure S20: **Temperature-dependent $\partial_z F_z(z)$ for an hBN/κ-ET interface.** At low temperatures and short tip-sample separations, Meissner repulsion is evident and decays gradually with increasing temperature. Near T_c (11.5 K) and at high tip-sample separations, background forces contribute significantly to the shape of the data.

13 Hyperbolic mode coupling to a BCS superconductor

Here, we consider the impact of hBN on a conventional superconductor. We use the standard Bardeen, Cooper and Schrieffer (BCS) theory to study the variation in superfluid density, assuming the hBN HMs couple linearly to an IR-active phonon responsible for the superconducting instability. This phonon will, in turn, couple either linearly or quadratically to the electron density. While κ-ET is not a conventional BCS superconductor, some intuition and qualitative insights may still be drawn from this calculation. In particular, we find below that whether the HMs enhance or suppress superconductivity is not generic but instead depends on the form of the electron-phonon coupling.

We start from a BCS Hamiltonian of the form

$$H = \sum_{k\sigma} \epsilon_k \hat{n}_{k\sigma} - V \sum_{kk'} c^\dagger_{k\uparrow} c^\dagger_{-k\downarrow} c_{-k'\downarrow} c_{k'\uparrow} \tag{31}$$

where ϵ_k is the single-particle dispersion, $V = g_0^2/\omega_D$ is the effective electron-electron interaction, g_0 is the electron-phonon coupling, and ω_D is the phonon Debye frequency. We work in units where $\hbar = 1$. We consider the electrons to be in the BCS ground state, given by

$$|\Psi_{\mathrm{BCS}}\rangle = \prod_k \left(u_k^* + v_k^* c^\dagger_{k\uparrow} c^\dagger_{-k\downarrow}\right)|0\rangle \tag{32}$$

where $2v_k^2 = 1 - \epsilon_k/E_k$ and the quasiparticle energy is $E_k = \sqrt{\epsilon_k^2 + \Delta^2}$. The coefficients satisfy the normalization condition $|u_k|^2 + |v_k|^2 = 1$, and the gap can be expressed in terms of known parameters as $\Delta = V \sum_k u_k v_k^*$. We denote the total energy of the superconducting state by E, and that of the normal state by $E_0 = 2\sum_{|\vec{k}|<k_F} \epsilon_k$. The difference between the BCS and normal state energies, $W = E - E_0$, can then be written (in the weak coupling limit $\hbar\omega_D \gg \Delta$) as

$$W = 2 \sum_{|\vec{k}|>k_F} \epsilon_k \left(1 - \frac{\epsilon_k}{E_k}\right) - \frac{\Delta^2}{V} \approx -2N(\epsilon_F)\Delta^2 \tag{33}$$

showing that the BCS ground state is stable. From BCS theory, we derive the zero-temperature gap $\Delta_0 = \Delta(T = 0)$ to be

$$\Delta_0 = 2\hbar\omega_D e^{-1/N(\epsilon_F)V} \tag{34}$$

The gap is related to the superfluid density by $|\Delta| = \sqrt{n_s}$, such that a suppression of the superfluid density is directly related to a suppression of the gap. In the following, we will calculate how the phonon-HM coupling modifies the effective interaction V and, by extension, the superconducting gap.

13.1 Phonon coupling to hyperbolic modes

To obtain the change in the gap due to coupling with the HMs, we consider the phonon-HM Hamiltonian

$$H_{\text{cav-ph}} = \sum_q \Omega_q a_q^\dagger a_q + \sum_q \omega_q b_q^\dagger b_q + \sum_q \lambda_q (a_q^\dagger + a_{-q})(b_{-q}^\dagger + b_q) \tag{35}$$

Here a_q is the annihilation operator for a phonon of frequency Ω_q, b_q is the annihilation operator for an HM of frequency ω_q, and $\lambda_q = Z_q l_q E_q$ is their coupling, where Z_q is the phonon Born effective charge, l_q the phonon oscillator length, and E_q the single-photon electric field amplitude of the HM. We assume that the mode volume used in the quantization procedure is finite, and therefore should be interpreted as an effective mode volume [Kamper Svendsen et al., arXiv:2312.17374]. The Hamiltonian has a block structure, such that we can write $H_{\mathrm{cav-ph}} = \sum_q \Phi_q^\dagger H_q \Phi_q$, with

$$H_q = \begin{pmatrix} \Omega_q & \lambda_q & 0 & \lambda_q \\ \lambda_q & \omega_q & \lambda_q & 0 \\ 0 & \lambda_q & \Omega_q & \lambda_q \\ \lambda_q & 0 & \lambda_q & \omega_q \end{pmatrix}, \quad \Phi_q^\dagger = \begin{pmatrix} a_q^\dagger & b_q^\dagger & a_{-q} & b_{-q} \end{pmatrix} \tag{36}$$

This Hamiltonian can be diagonalized by a Bogoliubov transformation, but to simplify the algebra, we first reformulate the Hamiltonian in terms of the canonical variables [Sentef et al., Sci. Adv. 4, eaau6969 (2018)]:

$$\begin{aligned} \hat{X}_q &= \frac{1}{\sqrt{2\Omega_q}}(a_{-q}^\dagger + a_q) \\ \hat{P}_q &= i\sqrt{\frac{\Omega_q}{2}}(a_{-q}^\dagger - a_q) \\ \hat{x}_q &= \frac{1}{\sqrt{2\omega_q}}(b_{-q}^\dagger + b_q) \\ \hat{p}_q &= i\sqrt{\frac{\omega_q}{2}}(b_{-q}^\dagger - b_q) \end{aligned} \tag{37}$$

Here and in the remainder of this section, we use uppercase (lowercase) letters to denote phonon (HM) coordinates and frequencies. In terms of these variables, we can write the Hamiltonian as

$$H_q = \frac{1}{2}\begin{pmatrix}\hat{P}_q & \hat{p}_q\end{pmatrix}\begin{pmatrix}1 & 0\\ 0 & 1\end{pmatrix}\begin{pmatrix}\hat{P}_q\\ \hat{p}_q\end{pmatrix} + \frac{1}{2}\begin{pmatrix}\hat{X}_q & \hat{x}_q\end{pmatrix}\begin{pmatrix}\Omega_q^2 & 2\lambda_q\sqrt{\Omega_q\omega_q}\\ 2\lambda_q\sqrt{\Omega_q\omega_q} & \omega_q^2\end{pmatrix}\begin{pmatrix}\hat{X}_q\\ \hat{x}_q\end{pmatrix} \tag{38}$$

It can be diagonalized by the transformation

$$\begin{aligned}\hat{x}_{\alpha,q} &= \cos\theta_q\,\hat{X}_q + \sin\theta_q\,\hat{x}_q = \frac{1}{\sqrt{2\epsilon_{\alpha,q}}}(\alpha_{-q}^\dagger + \alpha_q)\\ \hat{x}_{\beta,q} &= -\sin\theta_q\,\hat{X}_q - \cos\theta_q\,\hat{x}_q = \frac{1}{\sqrt{2\epsilon_{\beta,q}}}(\beta_{-q}^\dagger + \beta_q)\end{aligned} \tag{39}$$

where the mixing angle is $\tan(2\theta_q) = 2\lambda_q\sqrt{\Omega_q\omega_q}/(\Omega_q^2 - \omega_q^2)$, and the corresponding energies are

$$\begin{aligned}\epsilon_{\alpha,q}^2 &= \frac{1}{2}(\Omega_q^2+\omega_q^2) - \frac{1}{2}\sqrt{(\Omega_q^2-\omega_q^2)^2 + 16\lambda_q^2\Omega_q\omega_q}\\ \epsilon_{\beta,q}^2 &= \frac{1}{2}(\Omega_q^2+\omega_q^2) + \frac{1}{2}\sqrt{(\Omega_q^2-\omega_q^2)^2 + 16\lambda_q^2\Omega_q\omega_q}\end{aligned} \tag{40}$$

For future reference, we define the detuning parameter as the frequency mismatch between the phonon and the HM: $\delta_q = \Omega_q - \omega_q$.

13.2 Effective electron-electron interaction with linear electron-phonon coupling

Having obtained the coupled phonon-HM modes, we can write the electron-phonon coupling as

$$\begin{aligned}H_{e\text{-}ph} &= g_0\sum_{kq\sigma}(a_{-q}^\dagger + a_q)\,c_{k+q,\sigma}^\dagger c_{k\sigma}\\ &= g_0\sum_{kq\sigma}c_{k+q,\sigma}^\dagger c_{k\sigma}\left[\sqrt{\frac{\Omega_q}{\epsilon_{\alpha,q}}}\cos\theta_q(\alpha_{-q}^\dagger+\alpha_q) + \sqrt{\frac{\Omega_q}{\epsilon_{\beta,q}}}\sin\theta_q(\beta_{-q}^\dagger+\beta_q)\right]\end{aligned} \tag{41}$$

Here, $c_{k\sigma}$ is the annihilation operator for an electron with momentum k and spin σ, and g_0 is the electron-phonon coupling with units of energy. In systems with inversion symmetry, a linear coupling with momentum-independent electron-phonon coupling is forbidden for IR phonons, as these modes are odd under inversion. However, since the hBN/κ-ET interface breaks the inversion symmetry, such a coupling is allowed in the hybrid structure. We note that even with inversion symmetry a linear coupling is allowed if g_q is made slightly momentum-dependent (and odd), e.g. by taking $g_q = \mathrm{sign}(q)g_0$, which does not qualitatively change the subsequent discussion. Integrating out the phonon from Eq. 41 to obtain an effective electron-electron interaction, we find in the static ($\omega \to 0$) limit that

$$V_q = \Omega_q\frac{g_0^2\cos^2\theta_q}{\epsilon_{\alpha,q}^2} + \Omega_q\frac{g_0^2\sin^2\theta_q}{\epsilon_{\beta,q}^2} \tag{42}$$

Assuming that the phonon and HMs are weakly dispersing, we replace all momentum-dependent quantities with their momentum-averaged analogs. Identifying $\Omega = \omega_D$ and noting that $V_0 = g_0^2/\omega_D$, we calculate the difference $\Delta - \Delta_0$, with Δ obtained from the expression above. The result is shown in Fig. S21 (left-hand side); we find that the gap is always increased by the coupling to HMs.

13.3 Effective electron-electron interaction with quadratic electron-phonon coupling

As κ-ET is believed to be a non-BCS superconductor [Buzzi et al., Phys. Rev. Lett. 127, 197002 (2021)], we also discuss the effects of a quadratic electron-phonon coupling. We therefore consider an electron-phonon-HM Hamiltonian of the form

$$H = -t\sum_{ij\sigma}c_{i\sigma}^\dagger c_{j\sigma} + \Omega\sum_i a_i^\dagger a_i + \omega\sum_i b_i^\dagger b_i + \frac{\lambda}{2\sqrt{\Omega\omega}}\sum_i x_i X_i + gK\sum_i \hat{n}_i X_i^2 \tag{43}$$

where t is the nearest-neighbor hopping amplitude, $K = \Omega^2$ is the phonon spring constant, and g is a dimensionless constant. As discussed in [Kennes et al., Nat. Phys. 13, 479 (2017)], the effective electron-electron interaction for this model can be obtained from the energy difference $V = E(n=2) + E(n=0) - 2E(n=1)$, where $E(n)$ is the total energy of the system for fixed n. Note that for a particular n, the effective phonon frequency with the electron-phonon coupling taken into account is $\Omega(n) = \Omega\sqrt{1+2gn}$; thus, the effective interaction can be written as

$$V = \epsilon_\alpha(n=2) + \epsilon_\beta(n=2) + \epsilon_\alpha(n=0) + \epsilon_\beta(n=0) - 2\epsilon_\alpha(n=1) - 2\epsilon_\beta(n=1) \tag{44}$$

To obtain this interaction, we calculate the hybrid HM-phonon energies (Eq. 40) for each value of n, which is straightforward using the solution presented above. The resulting gap is shown in Fig. S21 (right-hand side). The quadratic coupling predicts a gap that is always decreased by the coupling to HMs.

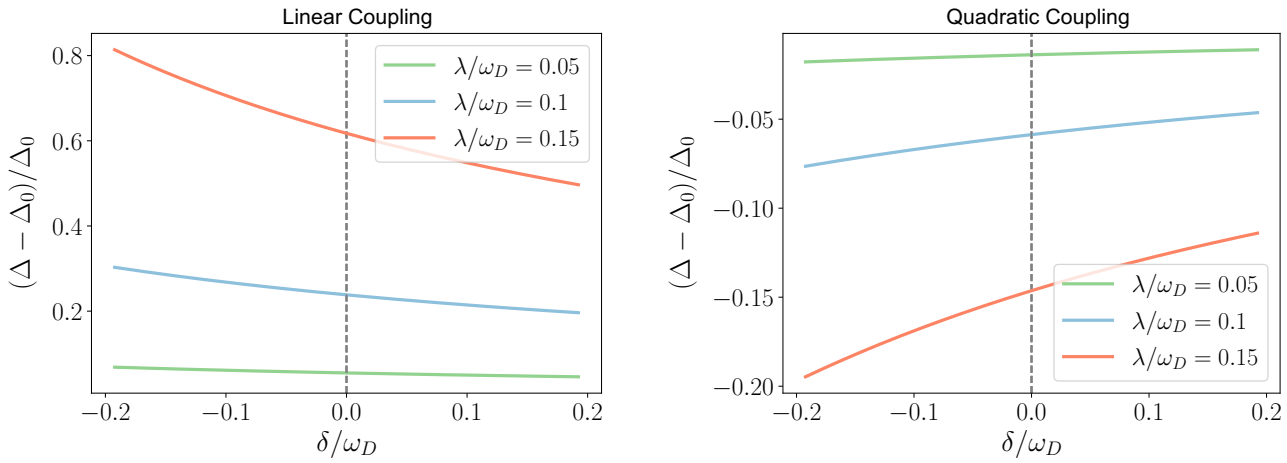

Figure S21: **Modification of the BCS superconducting gap due to coupling with HMs.** The relative change of the BCS superconducting gap, $(\Delta - \Delta_0)/\Delta_0$, as a function of the phonon-HM detuning δ (normalized by the Debye frequency), for various phonon-HM couplings λ. The left panel shows the result for the case of linear electron-phonon coupling, while the right panel shows the result for the case of quadratic electron-phonon coupling. The results were obtained using the following numerical values: For κ-ET, the critical temperature is $T_c = 11.5$ K. This leads to a zero-temperature BCS gap of $\Delta_0 = 1.76 k_B T_c = 1.74$ meV. For the Debye frequency, we use the C=C stretching mode frequency $\omega_D = 1470$ cm^{-1} $= 182$ meV. Writing the gap as $\Delta_0 = 2\hbar\omega_D e^{-1/N(\epsilon_F)V_0}$, we obtain $N(\epsilon_F)V_0 = 1/\log(2\hbar\omega/\Delta_0) = 0.19$.

14 Ruling out charge transfer

In the temperature-pressure phase diagram of κ-ET, the superconducting phase appears near a Mott insulator. The pressure axis can alternatively be explored with chemical pressure. The κ-(BEDT-TTF)$_2$Cu[N(CN)$_2$]Br compound is a hole conductor [McGuire et al., Phys. Rev. B 64, 094503 (2001)] residing near the optimal superconducting T_c [Kino and Fukuyama, J. Phys. Soc. Jpn. 65, 2158 (1996)]. It is thus likely that varying the carrier density would be detrimental to superconductivity. Such variations in carrier density may occur due to charge transfer. This effect should be much stronger at the RuCl$_3$/κ-ET interface than at the hBN/κ-ET interface. Charge transfer typically affects only a few layers of the crystal structure [Rizzo et al., Nano Lett. 20, 8438 (2020); Sternbach et al., Nano Lett. 23, 5070 (2023); Vitalone et al., ACS Nano 18, 29648 (2024)]. Thus, it cannot account for the suppression of superfluid density over hundreds of nanometers, but could influence a few nanometers near the κ-ET surface; this would manifest as a weak suppression of the Meissner force, much smaller than the effect we report in hBN/κ-ET heterostructures.

15 Reproducibility of the weak suppression over RuCl$_3$/κ-ET interfaces

The $\partial_z F_z(z)$ curve over the RuCl$_3$/κ-ET interface in Fig.1b are taken from Device 1. Here we show that this result is reproducible by measuring a $\partial_z F_z(z)$ curve over the RuCl$_3$/κ-ET interface of Device 5. Similarly to Fig. 1b, we observe almost indistinguishable curves, interpreted as a very weak suppression of the superfluid density at the RuCl$_3$/κ-ET interface. The curve is measured above the position where the maximal $\partial_z F_z$ signal was observed in Device 5 (see Fig. S13c).

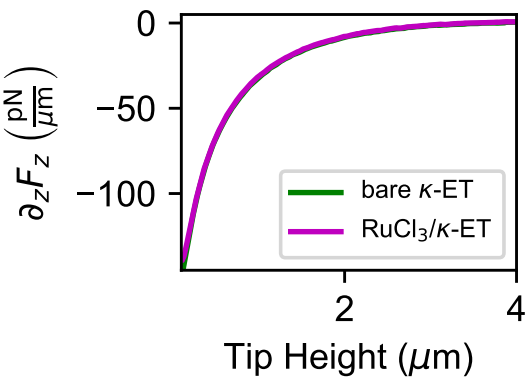

Figure S22: **$\partial_z F_z(z)$ for bare κ-ET and the RuCl$_3$/κ-ET interface of Device 5.** The green and magenta curves are measured over bare κ-ET and the RuCl$_3$/κ-ET interface of Device 5, respectively. The curves are nearly indistinguishable.